EC photon corrections and Covariance

Dustin Keller

(revised March 23, 2011)

Abstract

This note introduces an Electromagnetic Calorimeter (EC) reconstructed photon momentum correction method. The correction presented here can be implemented to all runs but there is minor sensitivity to EC energy calibration. It is therefore suggested that this method be repeated for the desired experiment. The reaction $\gamma p \to p\pi^-\pi^+\gamma$ is used to study the covariance of the photon using the EC in various kinematic ranges. Simulation accuracy is discussed along with relevant dynamical smearing techniques.

Contents

1 Introduction

Photon detection in CLAS through the Electromagnetic Calorimeter (EC) can make available or improve the analysis of many various reactions. Photons are separated from other neutral hits in EC by taking a high β cut. The β achieved through time-of-flight (TOF) can give a reasonable estimation for photon velocity when the EC time is calibrated with fast moving pions. A cut around $\beta \sim 0.9$ is usually a reasonable choice. The EC cluster position and energy reconstruction are then used to reconstruct the photon energy-momentum vector. This four-vector can then be used in combination with other decay products to study a large range of physics. A thorough CLAS study of the accuracy of the EC reconstructed four-vector for the photon in all kinematic ranges is presented here with the correlations between each measured variable resulting in the complete covariance matrix. The covariance information can give dynamic information about the quality of the kinematic variables achieve in various areas of the EC. These values can then be used to weight the EC photon measurements appropriately in constraint techniques that use a maximum likelihood method [1].

The EC has six triangular shaped sectors that fit together on the exterior of CLAS. Each sector consists of super layers made of alternating lead and scintillator strips that run parallel to the three U, V and W axes of the triangle. The light produced from a hit in the EC is measured in these three axes. The light travels through the scintillator and clear optical fibers to a photomultiplier tube producing an electric pulse. The pulse is sent through an analog-to-digital converter, so that the digital readout can be recorded. The irregularities in the scintillator, spacing of scintillator, and fibers are minimized during construction leading to the greatest contributions to the resolutions being the PMTs and EC geometry.

There are also resolution changes that are related to detector efficiency. Hits from the center of each triangular sector have improved measurements over those on the edges. There are effects of the torus coils and forward angles to be also considered. The EC consists of two main blocks, the inner consisting of 5 super layers of 3 scintillator layers (one from each view) for a total of 15 scintillator layers and the outer consisting of 8 super layers of 3 scintillator layers for a total of 24 scintillator layers. The difference in potential path length is of little concern in regards to photon energy reconstruction, however the distinction between the inner and outer block hits can help to create better understanding in the direction component resolutions.

There is some small fraction of photon hits that have a cluster reconstructed only in the outer block which have likely passed through holes in the inner EC block. The four-vector is constructed using the EC cluster position and the photon vertex. A study is done with respect to the different resolution parameters for each measured variable of the inner and outer blocks.

All possible combinations of momentum and position are studied to develop a complete understanding of the photon covariance of the electromagnetic calorimeter.

2 General Method

The reaction $\gamma p \rightarrow p\pi^-\pi^+\gamma$ is isolated in the g11a data set by selecting a proton a π^- and a π^+ with standard particle id techniques. With this charged particle topology there are several channel that contain a π^0 and a smaller amount that contain a single photon. To ensure that the photon topology is isolated a kinematically fitting to a missing photon hypothesis is compared to a kinematic fit to a missing π^0 hypothesis. All events with a greater confidence level of being a missing photon are preserved. A confidence level cut is implemented to ensure that all candidates have a confidence level less than 1% of being a π^0. Finally a confidence level cut greater than 15% of being a missing photon is used to isolate the best quality candidates. Fig. 1 shows the missing mass squared after the three step confidence level discrimination of the missing photon selection has been applied. The neutral particles in the EC are identified as clusters that are not associated with any charged track reconstructed from the drift chambers. The directional components of the photons reconstructed four-vector can have slight dependence on the particle id scheme. Ideally the photon vertex is used as the starting point of the vector and the cluster position in the EC is used as the termination point of the vector. The photon vertex can be obtain by knowing its production position using a charged particle form the same decay. For most runs the PART bank use the center of CLAS as the photon vertex position. SEB requires a charged particle used in the trigger to define the photon production point. Because the variation in the target length is usually small compared to the distance from the target to the EC, using the PART or EVNT bank to achieve the photon four-vector does not usually distort position resolutions significantly. In all cases a four-momentum correction is required for the best quality reconstructed photon. For the following example of four-vector cor-
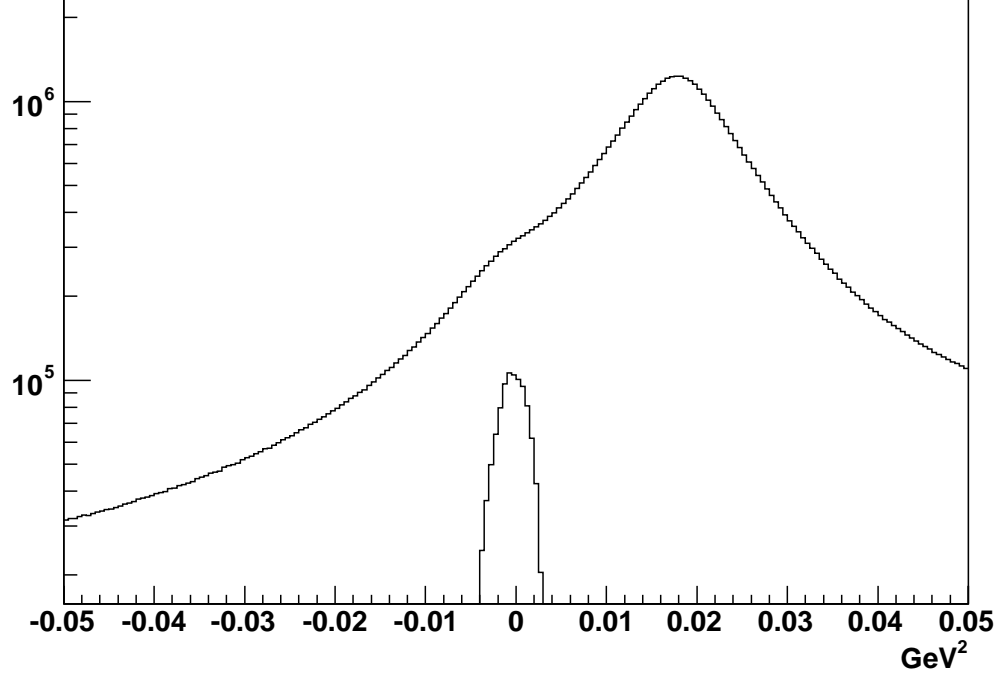
Figure 1: The missing mass squared of the detected proton, π^+, and π^-. Contamination from the overwhelming π^0 signal is avoided with the three confidence level cuts leaving only the missing mass of the photon. The photon counts used are seen at zero missing mass squared.

rections and covariance the PART bank was use to obtain the initial photon four-vector. This implies that a global sampling fraction has already been applied. For each event in the study there should be one detected photon to compare with each missing photon. The missing photon θ, ϕ, and p and the EC reconstructed θ, ϕ, and p can be compared to find the dynamic resolution over the EC face.

3 Photon Four-Momentum Correction

It is possible to implement a photon momentum correction by studying the trend found in momentum and position differences in the missing and detected values over various kinematic ranges. This is done by studying the residuals Δp, $\Delta \theta$, and $\Delta \phi$ over each dynamic variable p, θ, and ϕ. Δp is defined as the difference between the kinematically fit missing photon momentum and the reconstructed photon momentum. Likewise for the directional components $\Delta \theta$, and $\Delta \phi$. The missing photon four-vector is achieved by using the three confidence level cuts described in the previous section. After the best candidates are selected the tagged beam four-momentum and four-momentum of the charged particles are adjusted to meet the criteria of the missing photon hypothesis. Using these adjusted four-vectors the new ideal missing four-vector is found. To ensure the correct detected photon is analyzed a cut is made on the angle between the missing and detected three-vector of $\sim 2.86°$. The trend of the residuals should be distributed around zero, if it is not the mean of the distribution will display a trend that can be used to correct the measured variable. Once the photon momentum magnitude and directional residuals are evenly distributed around zero the missing and detected four-vectors are comparable. This implies that for the majority of events the detected photon momentum is the same within the experimental resolution as the high quality kinematically fit missing photon momentum.

Fig. 2 shows the Δp as a function of p in the top right. The distribution is binned and fit with a Gaussian in each bin to form a trend from the Gaussian means. The Gaussian means seen in the top right of Fig. 2 are then fit to a polynomial function f_1 of the dynamic variable p. This results in a correction to the magnitude of p of the form $p = p + f_1(p)$. This process is iterated until the mean is seen to be relatively flat with respect to the amplitude of the residual Δp. The resulting distribution after the correction is seen in the bottom left of Fig. 2 with the final means seen in the bottom right.

After the momentum magnitude correction is found and implemented similar corrections are applied to Δp with respect to ϕ such that $p = p + f(\phi)$, Δp with respect to θ such that $p = p + f(\theta)$, $\Delta \phi$ with respect to ϕ such that $\phi = \phi + f(\phi)$ and $\Delta \theta$ with respect to θ such that $\theta = \theta + f(\theta)$. No other corrections are required. Fig. 3 shows each of the mentioned residuals and Gaussian means before the corrections. Fig. 4 shows the same set of means after the polynomial functions where found in each case and implemented.

The Monte Carlo require separate corrections in the same variables. These corrections are necessarily applied to the Monte Carlo before any smearing to the photons four-vector is performed.

The same topology $\gamma p \to p\pi^-\pi^+\gamma$ can be used to demonstrate the effect of the correction by using the detec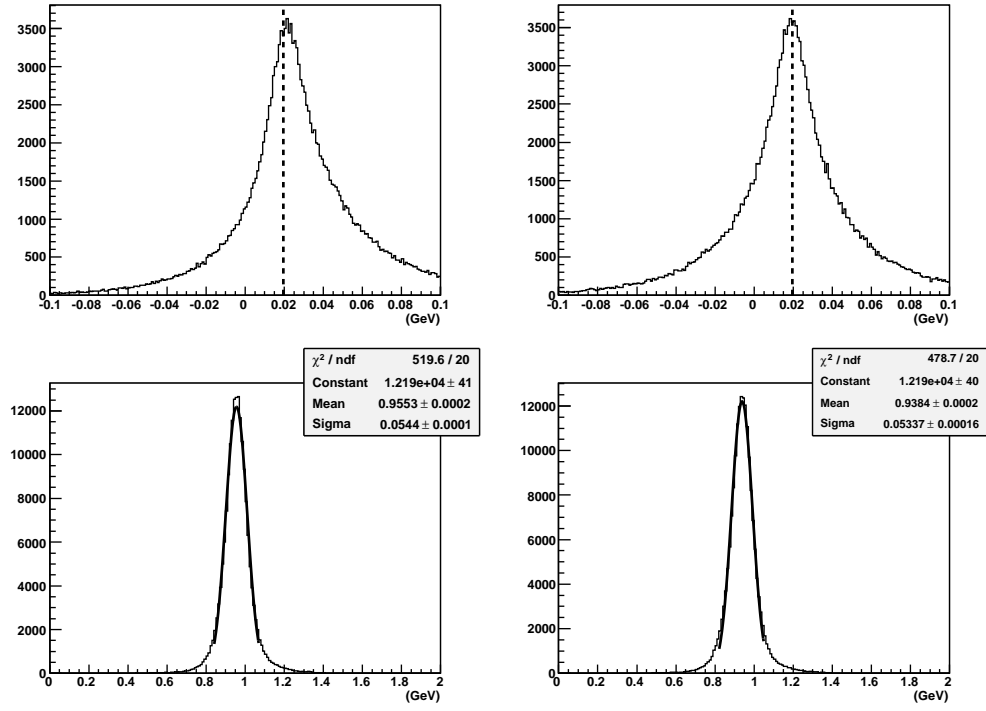ted photon to study the missing mass of the proton or pions. Fig. 5 shows the missing mass squared of the $\gamma p \to p\pi^+\gamma(\pi^-)$ with the PDG value for the pion mass at the dashed line before corrections (top left) and after (top right). The proton missing mass using $\gamma p \to \pi^-\pi^+\gamma(p)$ is also shown with a Gaussian fit before corrections (bottom left) and after (bottom right).
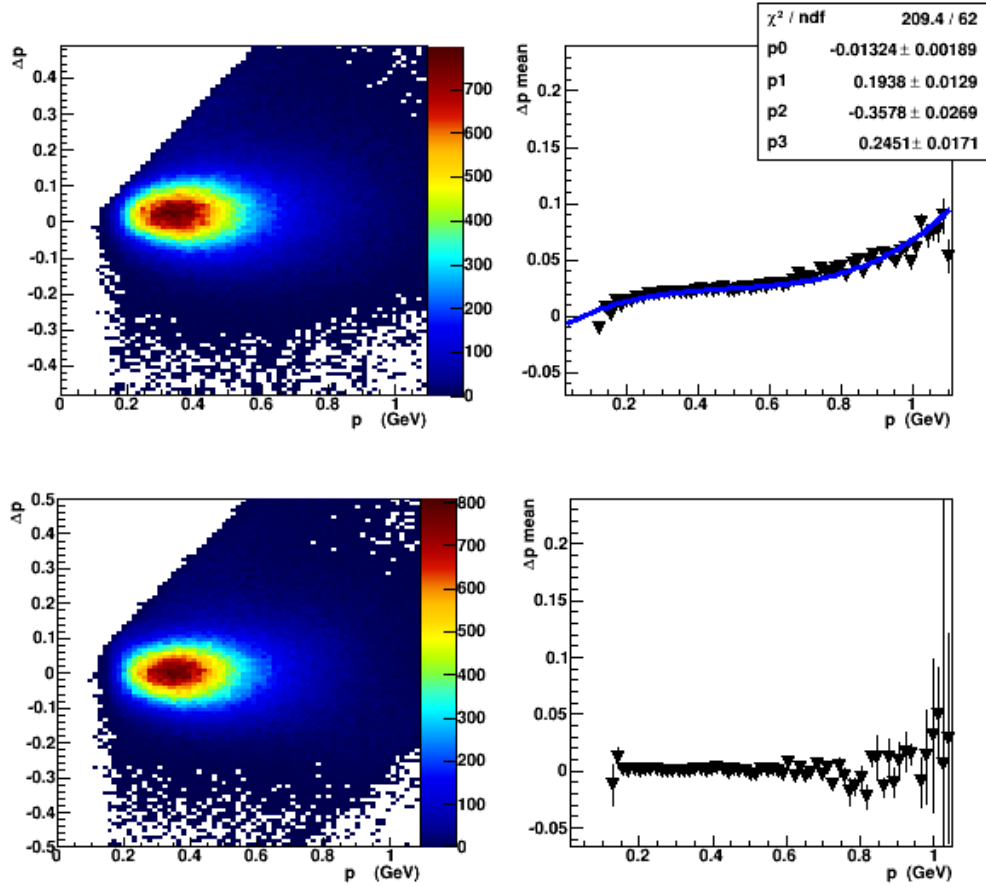
Figure 2: Top left: the Δp distribution before correction, top right: the Gaussian means from the binned fits, bottom left: the corrected distribution, and bottom right: the final corrected Gaussian means from the binned fits.
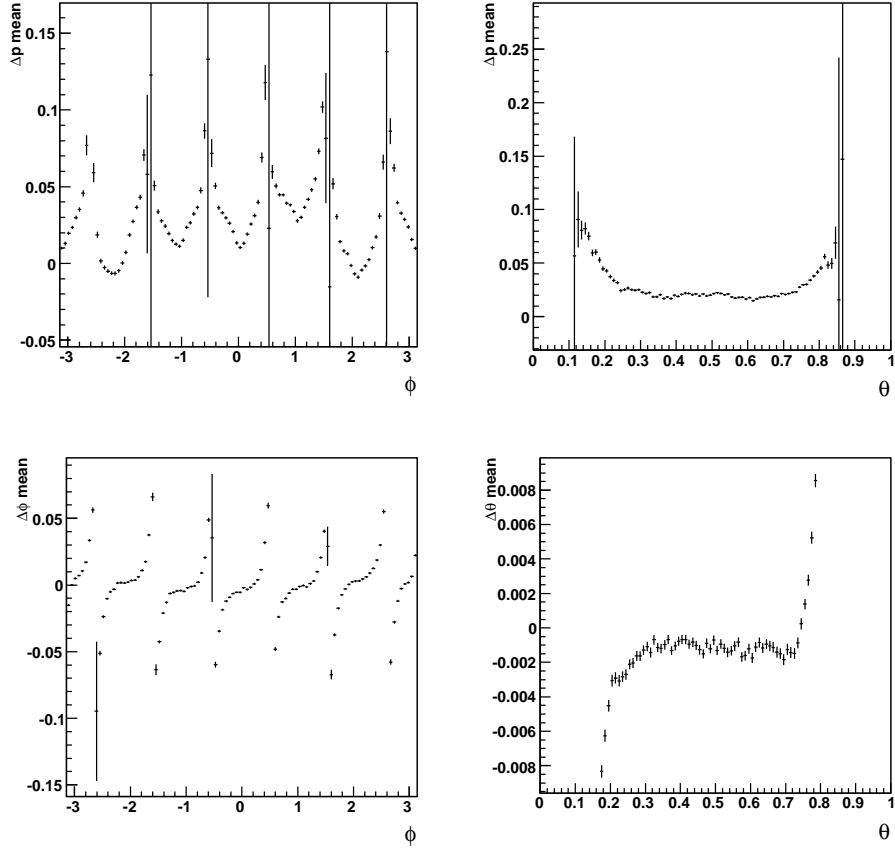
Figure 3: The Gaussian means for (top left) Δp with respect to ϕ, (top right) Δp with respect to θ, (bottom left) $\Delta \phi$ with respect to ϕ, and (bottom right) $\Delta \theta$ with respect to θ, before the angular corrections (after momentum magnitude correction with no fiducial cuts applied.)
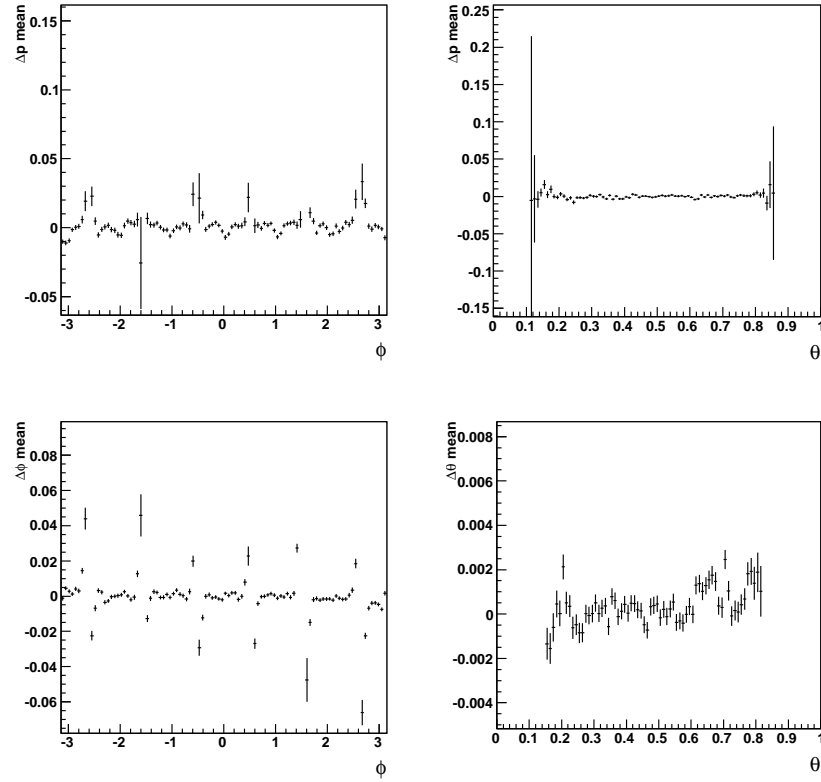
Figure 4: The Gaussian means for (top left) Δp with respect to ϕ, (top right) Δp with respect to θ, (bottom left) $\Delta \phi$ with respect to ϕ, and (bottom right) $\Delta \theta$ with respect to θ, after the corrections.

Figure 5: The missing mass squared of $\gamma p \rightarrow p\pi^+\gamma(\pi^-)$ with the PDG value for the pion mass at the dashed line before corrections (top left) and after (top right), and the missing mass of $\gamma p \rightarrow \pi^-\pi^+\gamma(p)$ with a Gaussian fit before corrections (bottom left) and after (bottom right).

4   Photon Resolutions

(a) cosθ vs ϕ (missing γ)   (b) cosθ vs ϕ (detected γ)
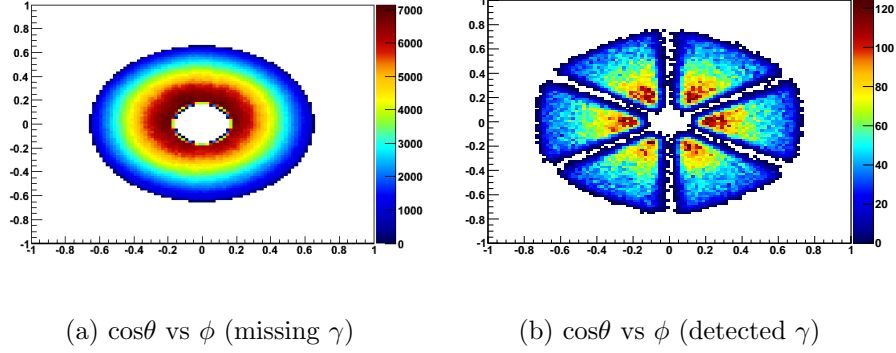
Figure 6: Demonstration of θ vs ϕ for the (a) missing photon and (b) the detected photon.

The structure of CLAS prevents photons from being detected with the same precision in all directions. The six superconduction coils in front of the EC limit its range in ϕ. The difference between the missing photon (a) and the detected photon (b) reconstructed position over the face of the EC can be seen in Fig. 6. The resolution for the photon in the EC changes according to its kinematic range and EC geometry so again the kinematically fit missing photon four-vector is used to study the residuals to obtain the variance σ for each measured variable over all dynamic parameters as defined in the target frame. Fig. 7 shows $\Delta\phi$, $\Delta\theta$, and Δp over a range of the momentum magnitude, ϕ, and θ used in the resolution studies for the $g11a$ data set.

Once the residuals (Δx) are obtained for data and Monte Carlo the distributions with respect to p, θ and ϕ are sliced and binned in each dynamic variable. Each bin is projected onto the Δx axis and fit with a Gaussian to find the (σ_x) resolution for that bin. The Gaussian mean for each fit should now be centered around zero implying good photon reconstruction and correction in the corresponding variable. Fig. 8 show the (top) missing momentum against the EC reconstructed momentum after all corrections and the (bottom) energy resolution σ/E for photons over the same energy range with a linear fit. The momentum comparison indicates a very reasonable match leading to a realistic depiction of the energy resolution for the photon.

Figs. 9-17 shows the results of the resolution extraction for the $g11a$ data. Figs. 18-26 shows the results of the resolution extraction for the Monte Carlo prior to any smearing. In each case the upper left plot shows the number of events per bin used. The upper right plot shows the mean from the Gaussian fits. The lower left plot shows the values of σ from the Gaussian fits over the required dynamical range. The lower right plot shows the χ^2 from each Gaussian fit for every bin used.

5 Photon Covariance

To use this information to construct a dynamic covariance matrix for EC detected photons first consider the changes seen in Figs. 9-11. The momentum resolution σ_p changes significantly for various values of momentum reaching about $\sigma_p \sim 0.15$ for $p = 0.8$. The changes in σ_p over θ and ϕ are much smaller but still to large too ignore. The $\sigma_p(\theta)$ plot in Fig. 10 show that the momentum resolution is larger for small θ ranging from 0.05 to ~ 0.15. It is also seen in Fig. 11 that there are small changes from sector to sector. Naturally there will be fewer hits on the edges of each EC sector indicated by the larger error bars in $\sigma_p(\phi)$ around those areas. It is necessary to determine if counts from these regions should be removed or have less weight in an analysis. Three linear cuts in can be made so that these problematic zones are eliminated. The regions can be define using the directional components of the momentum vector $\hat{p}_y = -\sqrt{3}/3\hat{p}_x \pm d/\cos(30)$, $\hat{p}_y = \sqrt{3}/3\hat{p}_x \pm d/\cos(30)$, and $\hat{p}_x = \pm d$, where d is the width of the low acceptance region $d \sim 0.073$, seen if Fig 6(b). The value of d is selected here to be cutting into the edge of the scintillator enough for fringe effects to be completely removed. For the present application no EC fiducial cuts are implemented to allow these region to be included in the covariance study. Based on σ_p the resolutions are chosen to be studied in several θ and ϕ bins. To study the resolution sector by sector, six ϕ bins are selected with respect to the geometry of each triangular region. The change in σ_p is binned over the angle $\theta \epsilon (0.1, 0.8)$ which is divided into 7 bins. It is then possible to again slice and bin the data fitting to several Gaussians to find the trend in σ. The momentum resolution can then be expressed as a functional of $\vec{p}$ and each bin of $\sigma_p(p, \theta, \phi) = \sigma_p(p)|_{\theta, sector}$ can be fit with a second order polynomial that can be used to represent the momentum variance term in the dynamic covariance matrix. A quadratic fit is used over the momentum range of 0.1-

1.15 GeV. This range represents the majority of the photons corresponding to the phase space for the reaction $\gamma p \to p\pi^-\pi^+\gamma$. Fig. 27 shows each sector before dividing into θ bins. Fig. 28 shows each sector before dividing into θ bins with photon events hitting either the inner EC layer or the inner and outer combined. Fig. 29 shows each sector before dividing into θ bins with photon events hitting only the outer EC layer. If there is a large number of these events in the data sample in can be an indication of a problem in how the event was reconstructed. Usually only a small fraction of events ($> 5\%$) will pass the inner block completely. In some cases it may be safer to cut out these problematic events. For the sake of completeness these events are included in the study but differentiated. The plot and fit in each sector and θ bin are shown in Figs. 30-36.

Dynamic empirical smearing [2] is then performed on the Monte Carlo momentum in each of the same sector and θ bins. The resulting momentum resolutions are shown in Figs. 37-43. More about this smearing technique is discussed in Section 6.

The trend in σ_θ shown in Fig.12 demonstrates $\sigma_\theta(p)$ changes between 0.017-0.025 which are small variations but larger than the changes seen in the $\sigma_\theta(\phi)$, ($\sigma_\theta(\theta)$) trends seen if Fig. 14, (Fig. 13). The variance σ_θ can then just be dynamically represented by the trend in $\sigma_\theta(p)$. A fourth order polynomial is used to fit the trend to use as the dynamic representation of the θ variance term which is shown in Fig. 44.

The trend in σ_ϕ shown in Fig.15 also demonstrates $\sigma_\phi(p)$ visible changes as do $\sigma_\phi(\theta)$, however $\sigma_\phi(\phi)$ remains relatively flat. The variance σ_ϕ can be dynamically represented by binning $\sigma_\phi(\theta)$ in four momentum ranges. One could have just as easily binned $\sigma_\phi(p)$ in several θ bins. A fourth order polynomial is used to fit the trend to use as the dynamic representation of the ϕ variance term which is shown if Fig. 45 for each momentum range. The upper left plot shows the values of σ from the Gaussian fits over the full momentum range while the upper right shows the same for momentum from 0-0.5. The bottom left shows the momentum range 0.5-0.85, and the bottom right shows from 0.85 and up.

6   Dynamic Empirical Smearing

Once the EC photon momentum corrections are obtained for both the data and Monte Carlo it is necessary to accurately match the Monte Carlo reso-

lutions to that of the data. This is done by applying a dynamic empirical smearing to Monte Carlo measured variables p, θ, and ϕ to accurately represent $\sigma_p(p)$, $\sigma_\theta(p)$, and $\sigma_\phi(\theta)$ seen in the data. The trends and magnitude can be experiment dependent. Each measured parameter is smeared out according to the dynamical variable by sampling from a Gaussian with the corresponding width (σ_{smear}) to match the data resolution. The σ_{smear} from the Gaussian is usually a function of one or more kinematic variables.

Integrating over all sectors and θ bins the general smearing required for the photon momentum magnitude can be described as,

$$p_f = p_i + 0.32 p_i^2 e^{-p^2/2\sigma_{smear}^2(p_i)} \tag{1}$$

where $\sigma_{smear}(p_i)$ is

$$\sigma_{smear}(p_i) = 0.0122 p_i^2 - 0.011 p_i - 0.0027. \tag{2}$$

In this notation p_i is the initial Monte Carlo reconstructed momentum magnitude and p_f is the momentum magnitude after smearing. The function for $\sigma_{smear}(p)$ is found by studying the difference in Monte Carlo and data of σ_p over the variable p. Without any dynamical change in the Monte Carlo it is as easy as fitting the trend of the resolutions seen in the data with a polynomial and using the results to correct the Monte Carlo in $\sigma_{smear}(p)$. Each Sector and θ bin have a unique $\sigma_{smear}(p)$ and are adjusted accordingly. Using this method the Monte Carlo resolutions are tuned to fit very closely to the data so that the covariance matrix is equivalent for all practical purposes.

A similar procedure can be used for the directional components $\sigma_\theta(p)$ and $\sigma_\phi(\theta)$ however it is found that the resolutions of the directional variables are well represented and no further smearing is required.

7   Correlations

The photon parameter correlations between the measured variables are used to obtain the off diagonal terms of the covariance matrix as described in Ref. [1]. The Pearson correlation is shown for each CLAS sector for $\rho_{p\theta}$ in Fig. 46, $\rho_{p\phi}$ in Fig. 47, and $\rho_{\phi\theta}$ in Fig. 48. These same correlations are used in the Monte Carlo covariance.

8 Conclusion

From these results it is possible to build a photon EC covariance matrix with the reported resolutions and correlations as an estimate for the detectors dynamical kinematic uncertainties. The reported resolutions require that the EC reconstructed photon four-momentum start are CLAS center. Knowing the photons interaction vertex only results in slight changes to the direction components of the resolutions reported here. Also the reported dynamical resolutions can be used without fiducial cuts in EC detection which enables higher statistics in analysis. This is verified by using the full angular range of the EC and kinematically fitting the topology $\gamma p \rightarrow \pi^- \pi^+ \gamma(p)$ using the photon covariance mapped out above. The Pull distributions for each measured variable of the π^-, π^+, and γ are within reason without the fiducial cuts, see Fig. 49. The confidence level distribution is very flat and the χ^2 distribution displays the form of the probability density function for a single degree of freedom. Combined these provide a good quality checks for the newly developed covariance matrix.
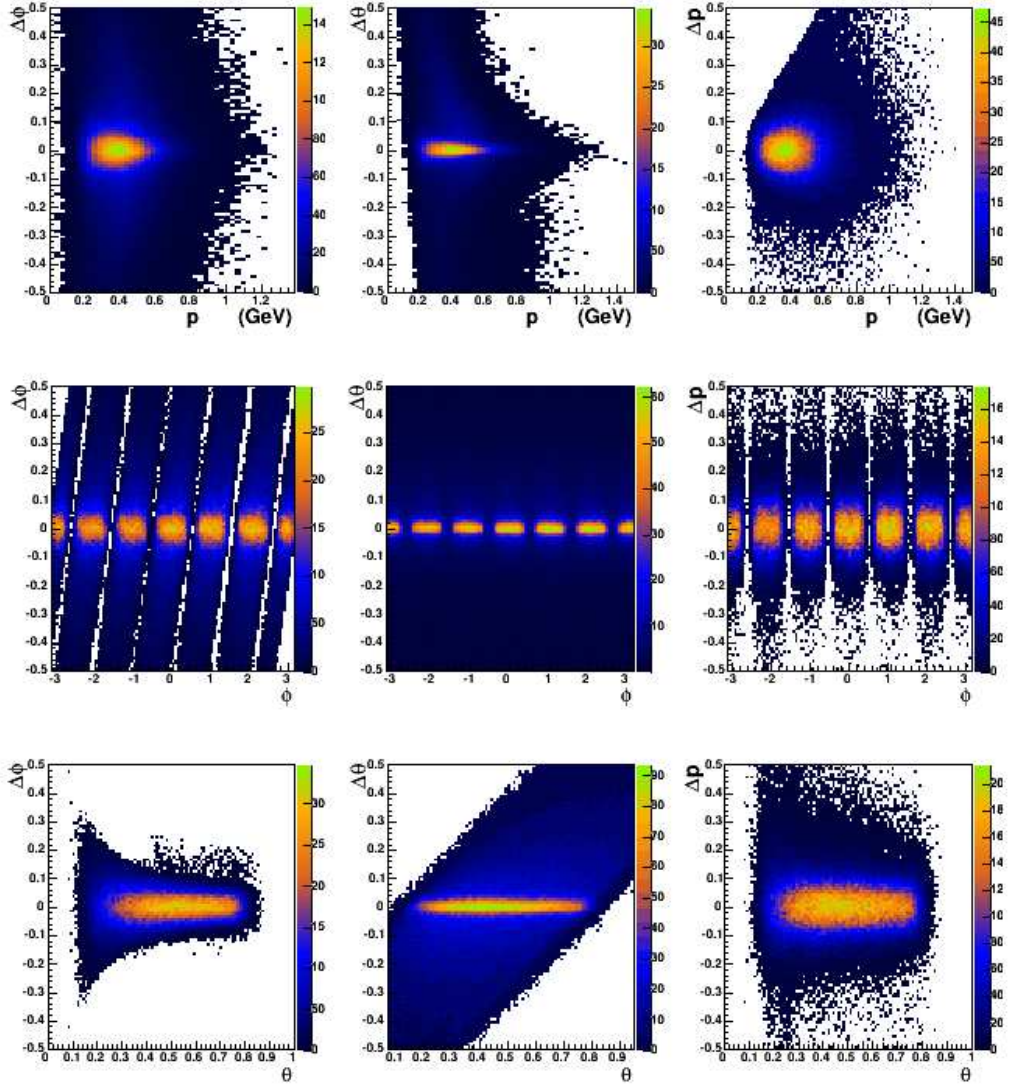
Figure 7: The $g11a$ data set is used to obtain $\Delta\theta$, $\Delta\phi$, and Δp (upper left), over a range of p, ϕ, and θ in each case (units are GeV and radians).
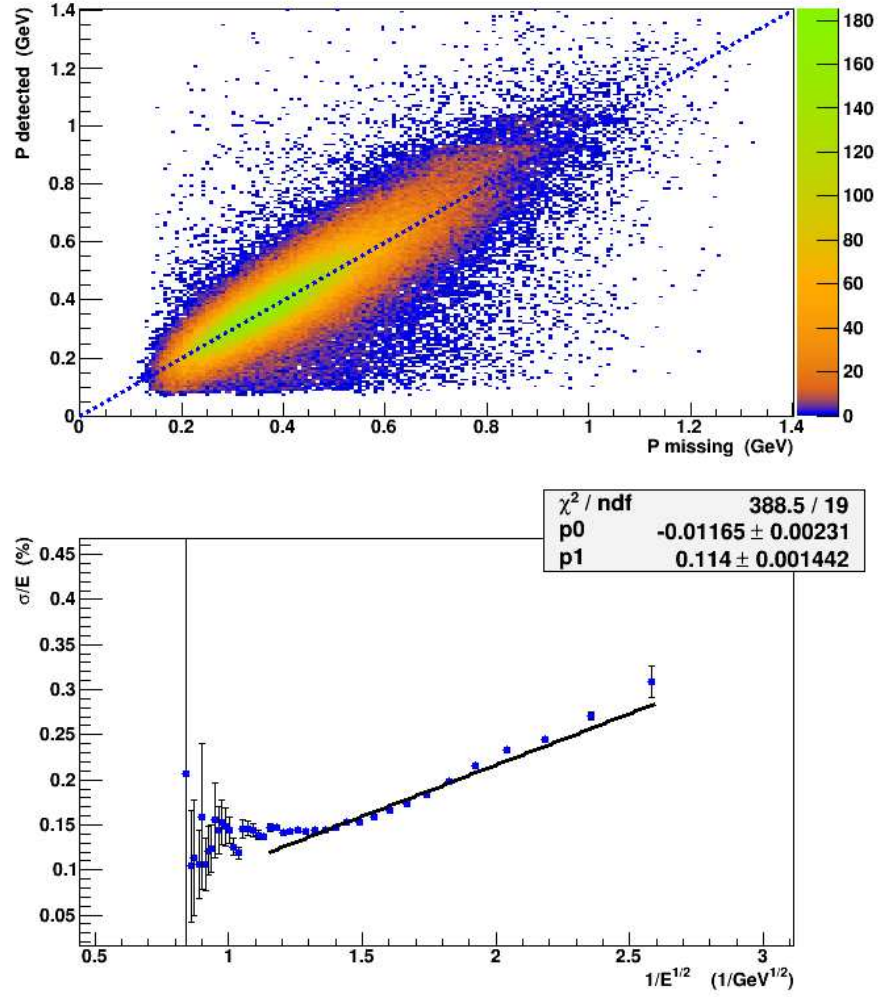
Figure 8: The (top) missing momentum against the EC reconstructed momentum after all corrections and the (bottom) energy resolution σ/E for photons over the same energy range with a linear fit.
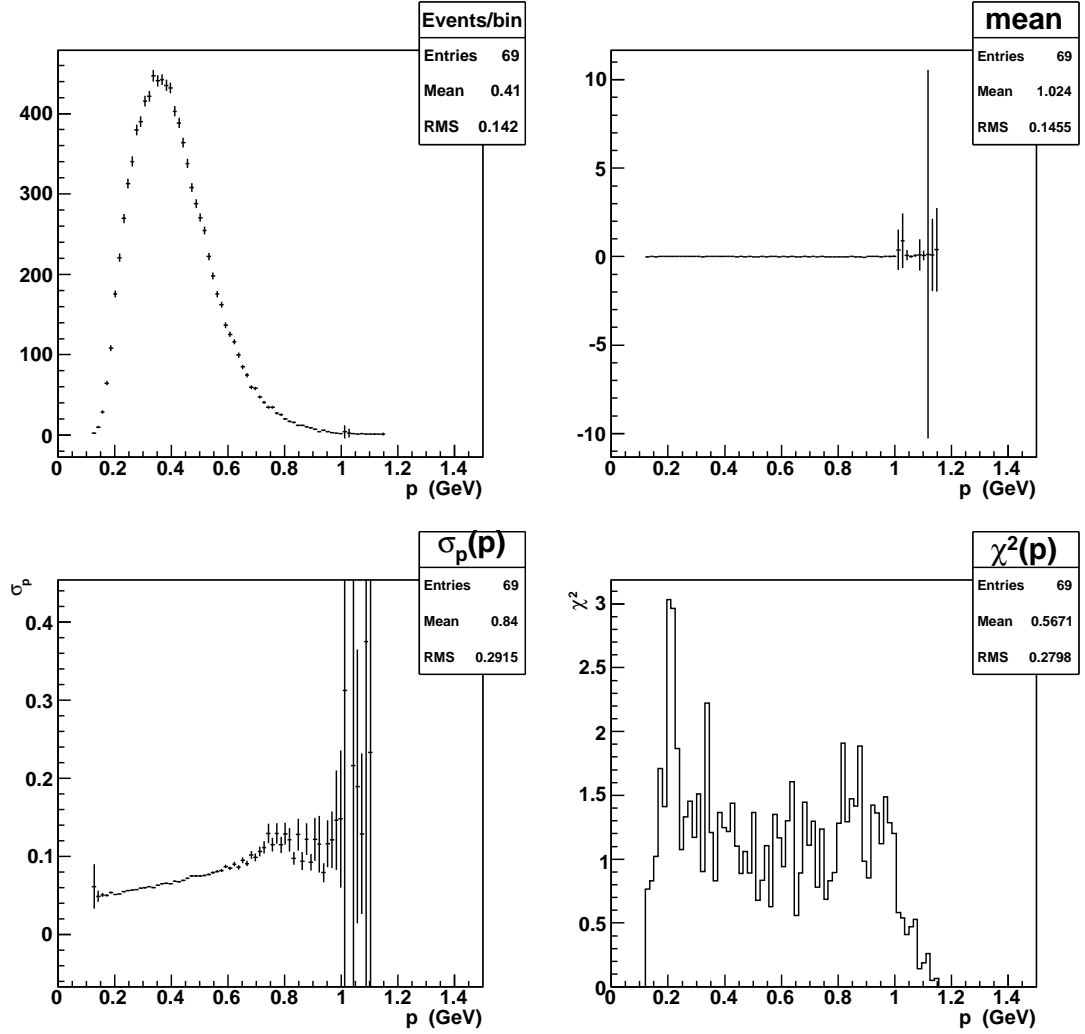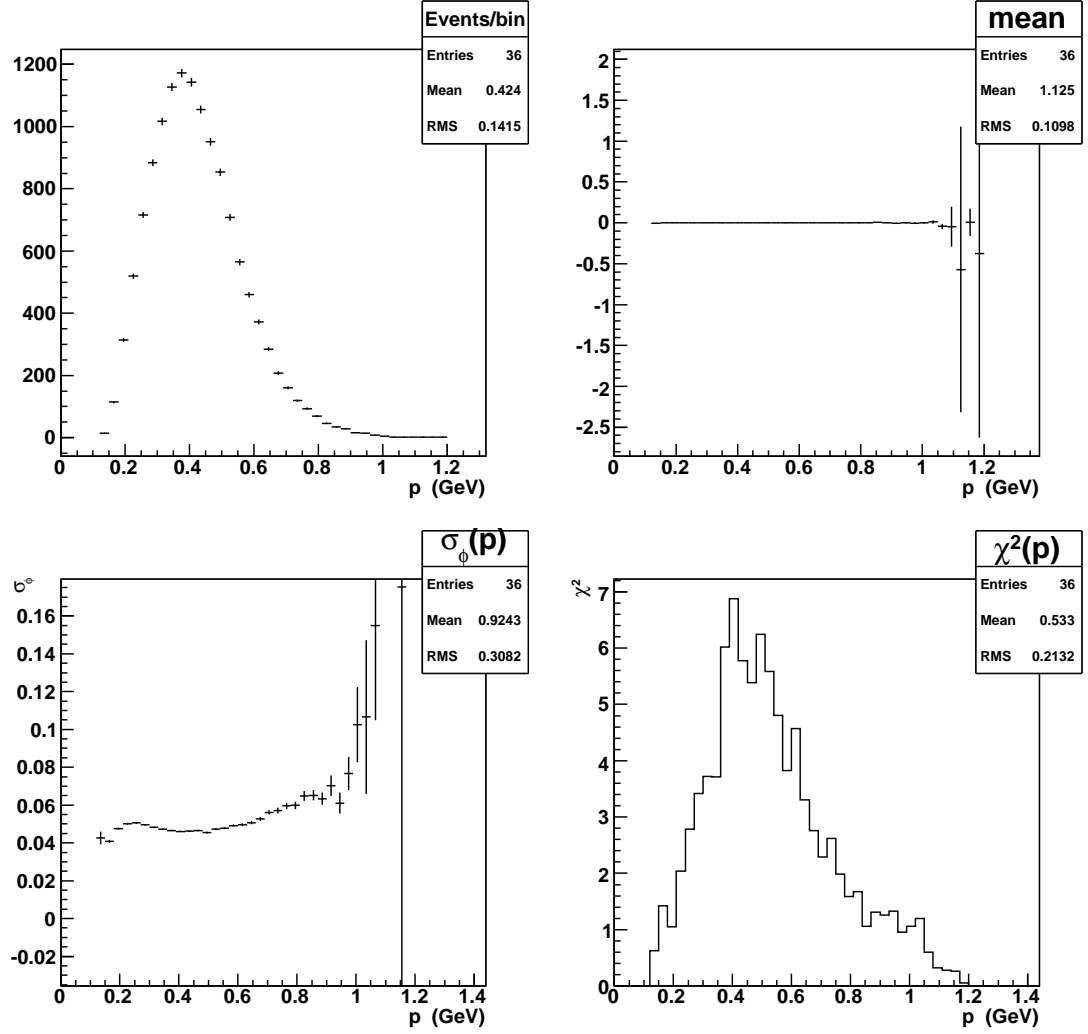
Figure 9: The $g11a$ study of $\sigma_p(p)$. The upper left plot shows the number of events per bin used. The upper right plot show the mean from the Gaussian fits. The lower left plot shows the values of σ from the Gaussian fits over the required range of p. The lower right plot shows the χ^2 from each Gaussian fit for every bin used.
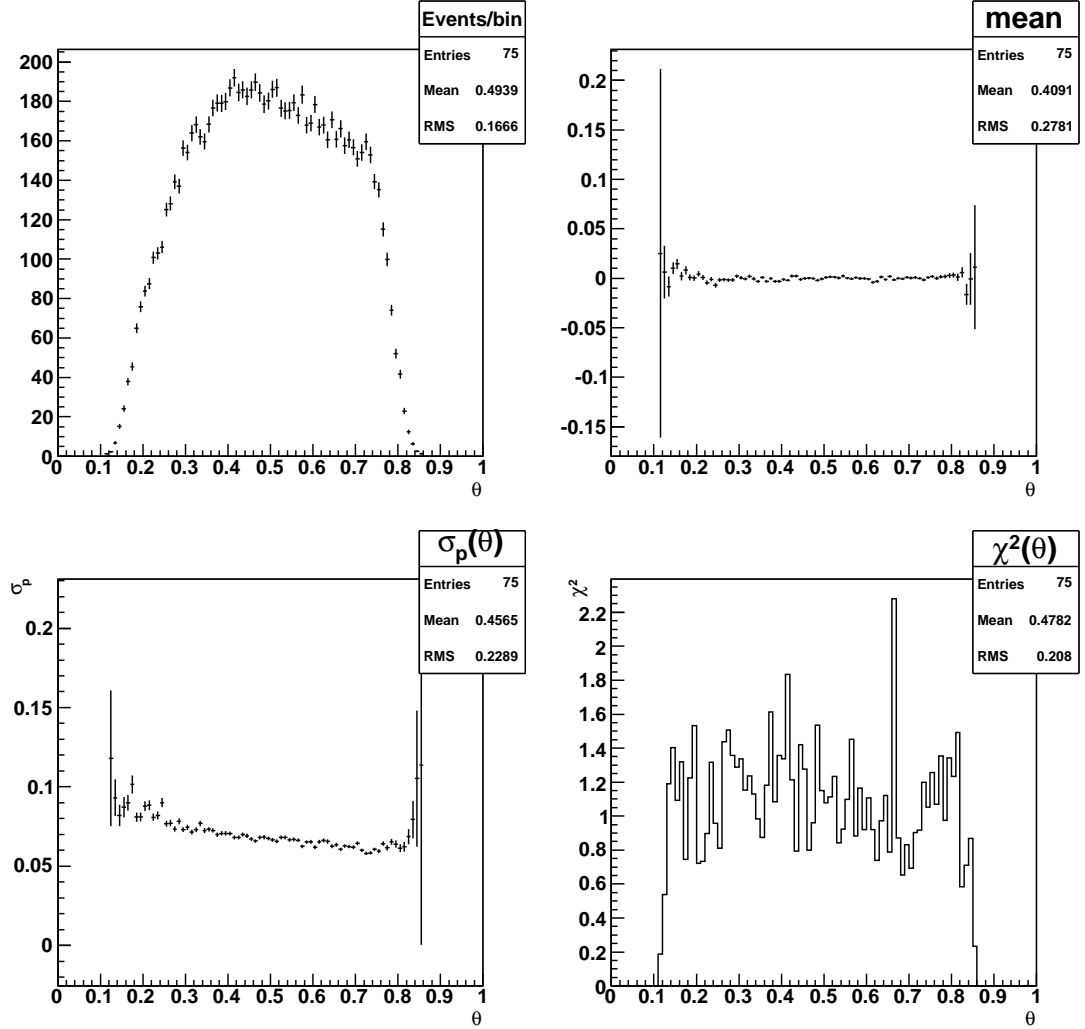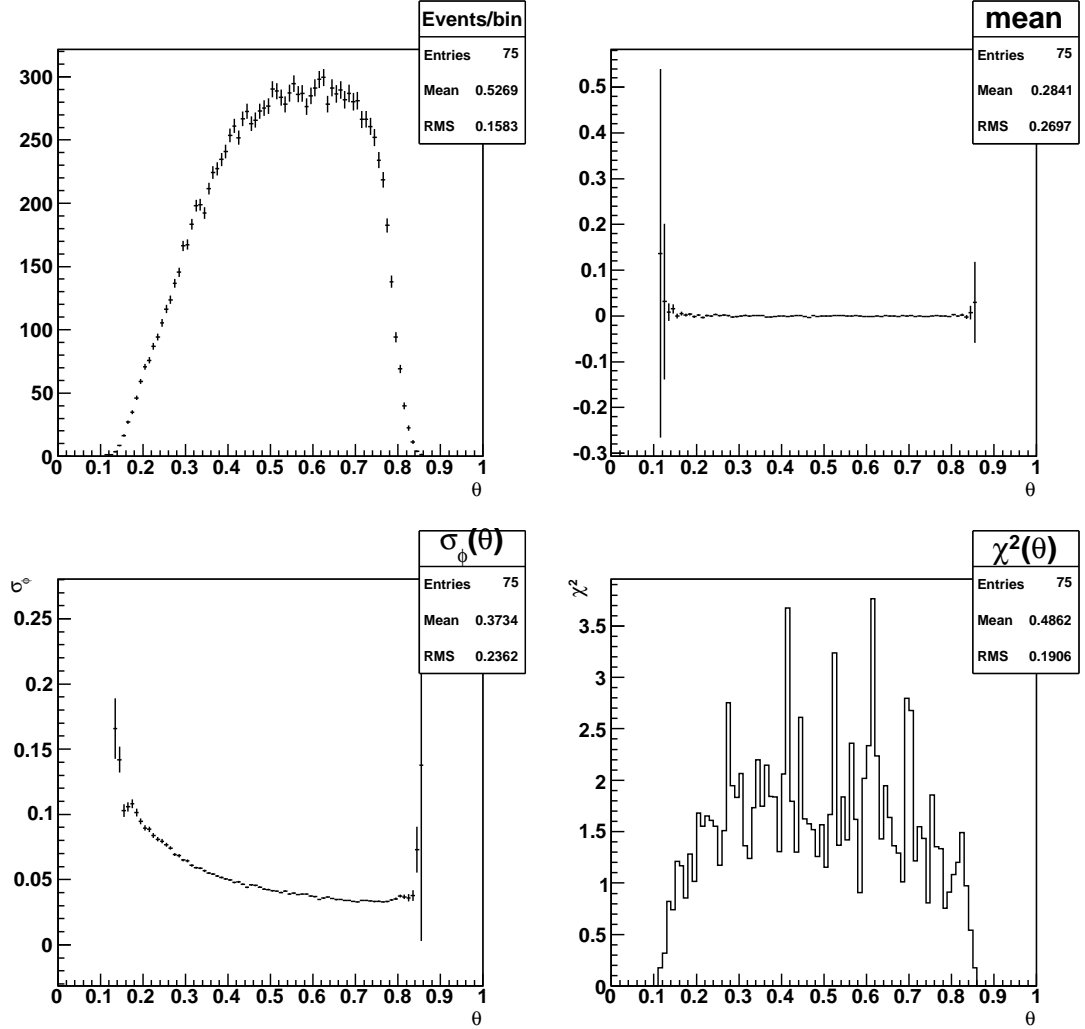
Figure 10: The $g11a$ study of $\sigma_p(\theta)$. The upper left plot shows the number of events per bin used. The upper right plot show the mean from the Gaussian fits. The lower left plot shows the values of σ from the Gaussian fits over the required range of θ. The lower right plot shows the χ^2 from each Gaussian fit for every bin used (angular units are radians).
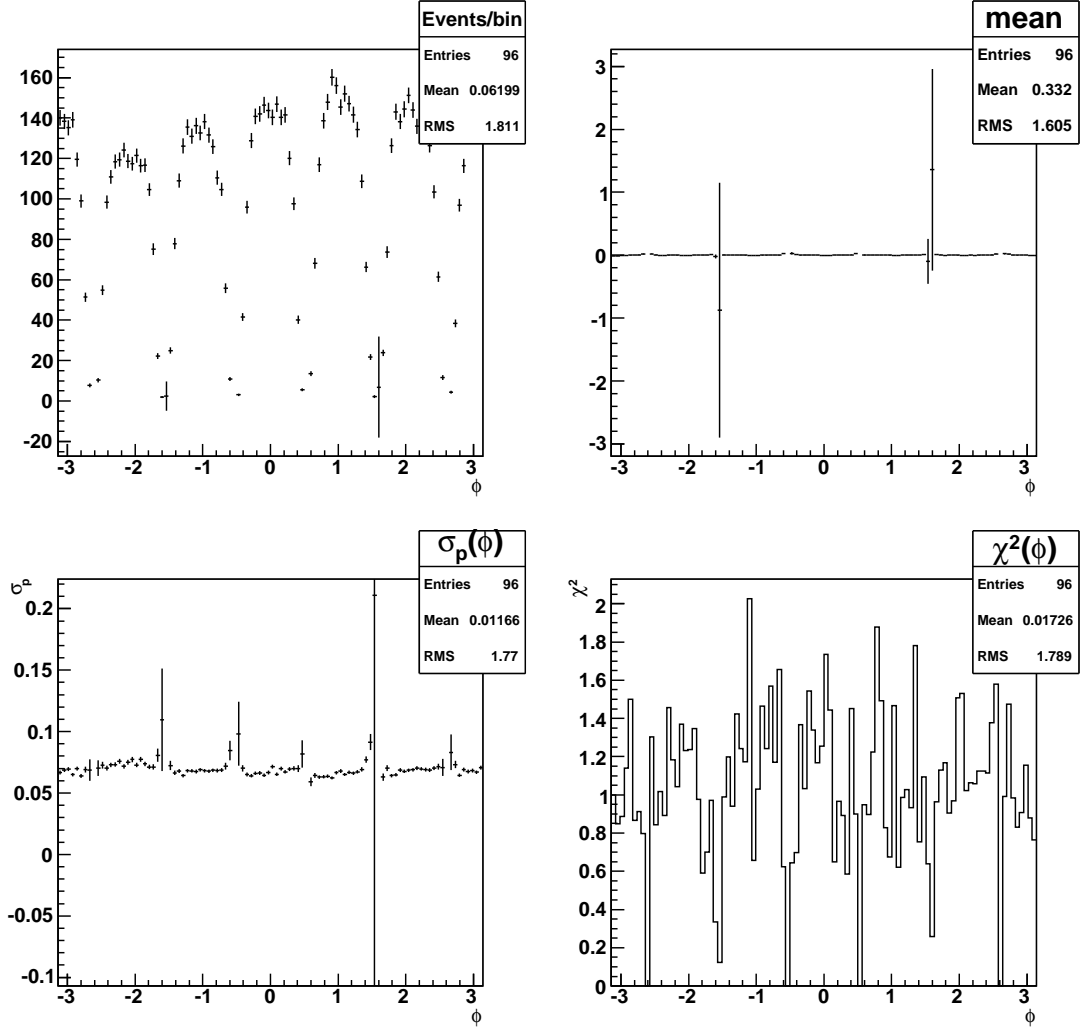
Figure 11: The $g11a$ study of $\sigma_p(\phi)$. The upper left plot shows the number of events per bin used. The upper right plot show the mean from the Gaussian fits. The lower left plot shows the values of σ from the Gaussian fits over the required range of ϕ. The lower right plot shows the χ^2 from each Gaussian fit for every bin used (angular units are radians).
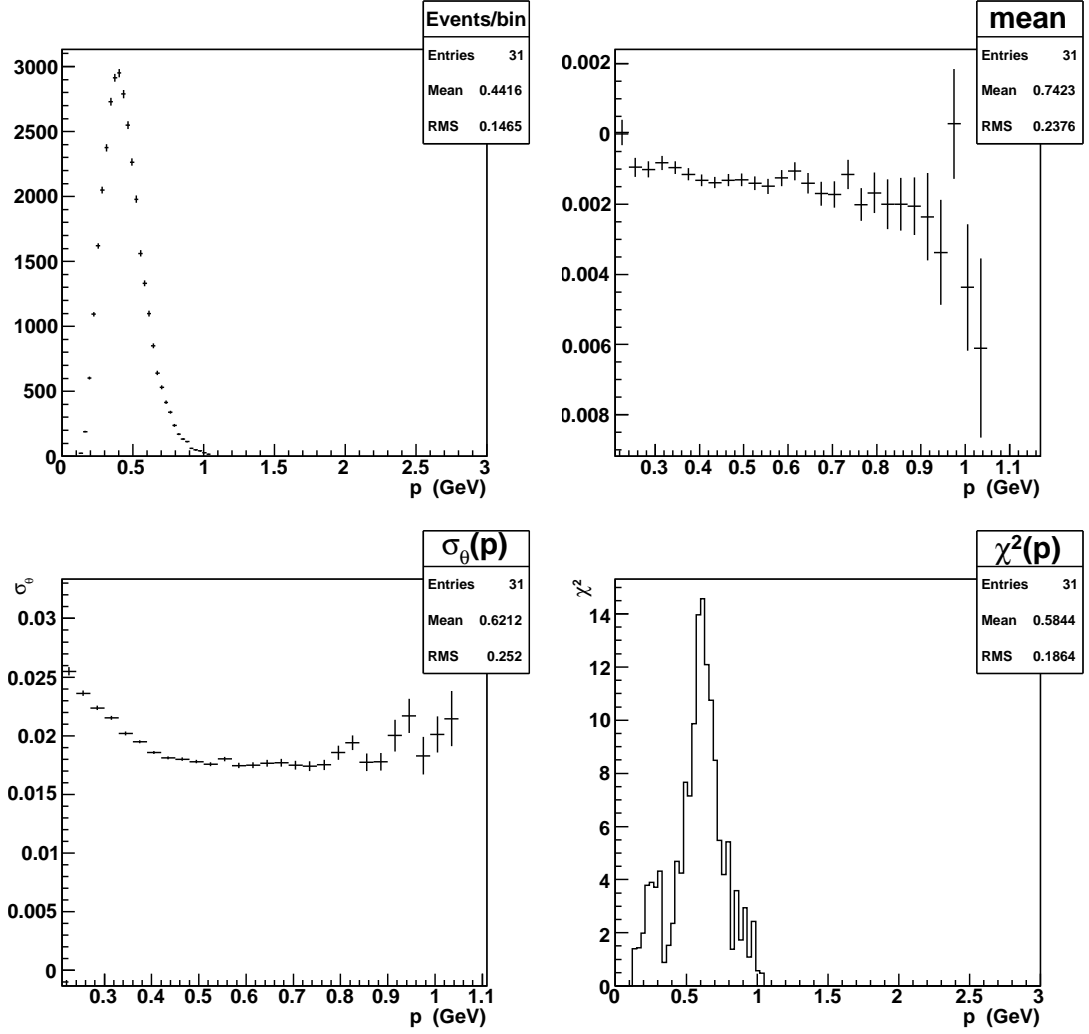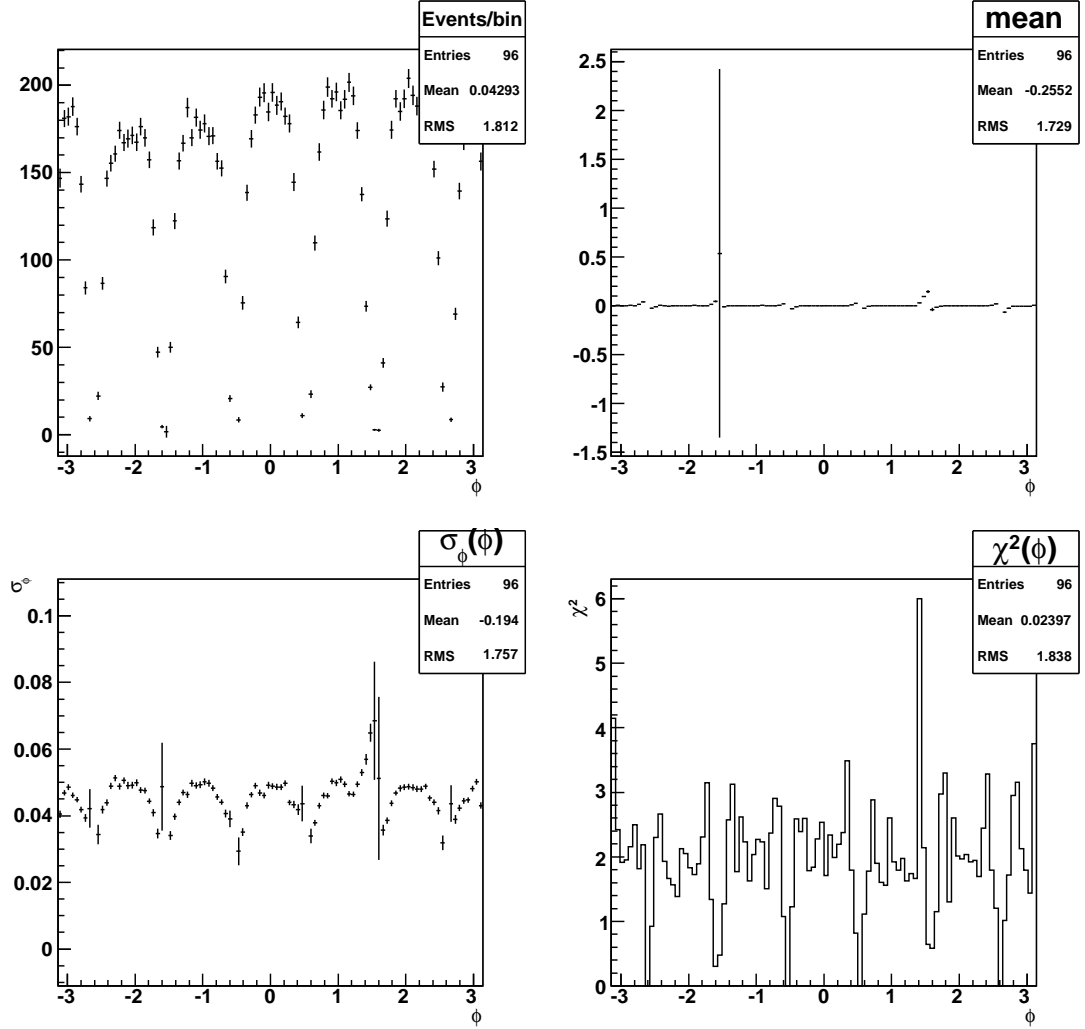
Figure 12: The $g11a$ study of $\sigma_\theta(p)$. The upper left plot shows the number of events per bin used. The upper right plot show the mean from the Gaussian fits. The lower left plot shows the values of σ from the Gaussian fits over the required range of p. The lower right plot shows the χ^2 from each Gaussian fit for every bin used (angular units are radians).
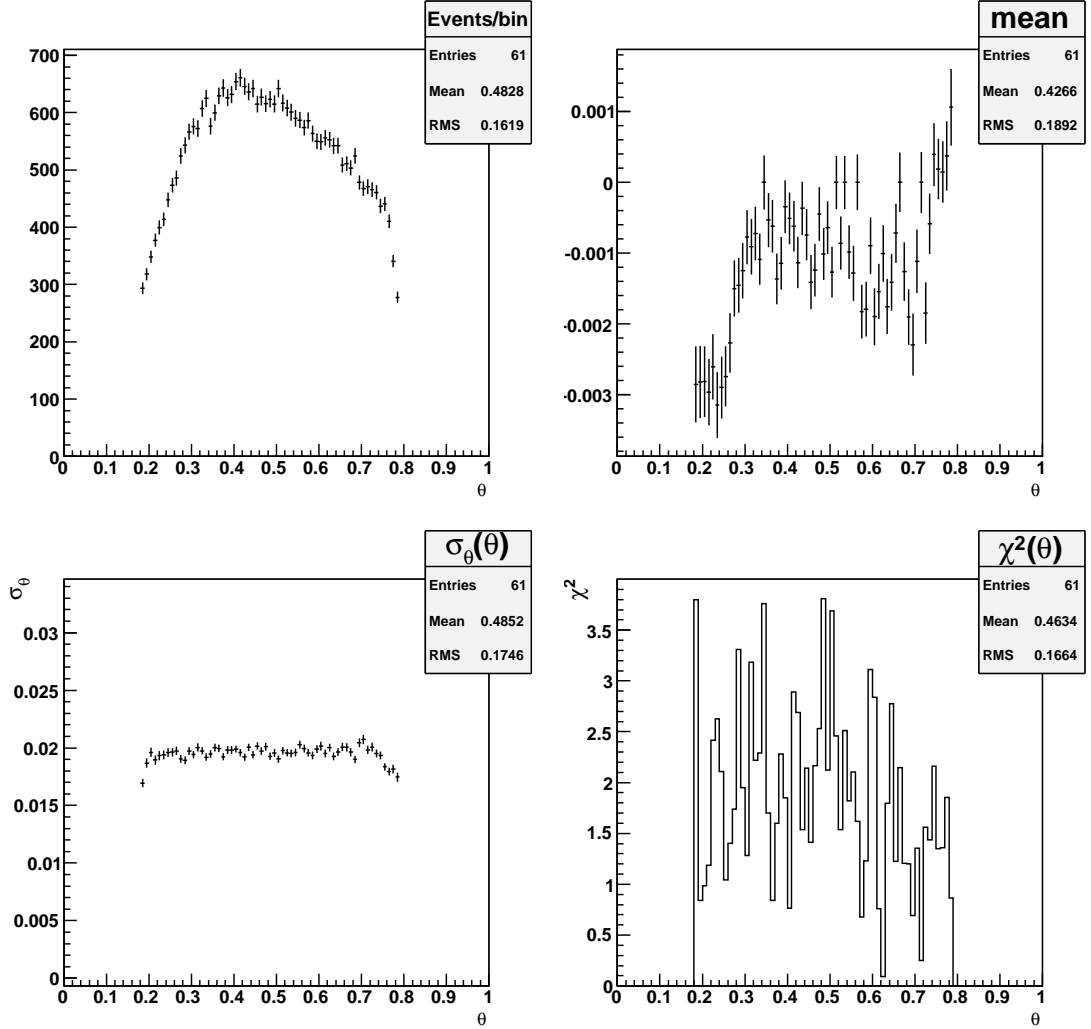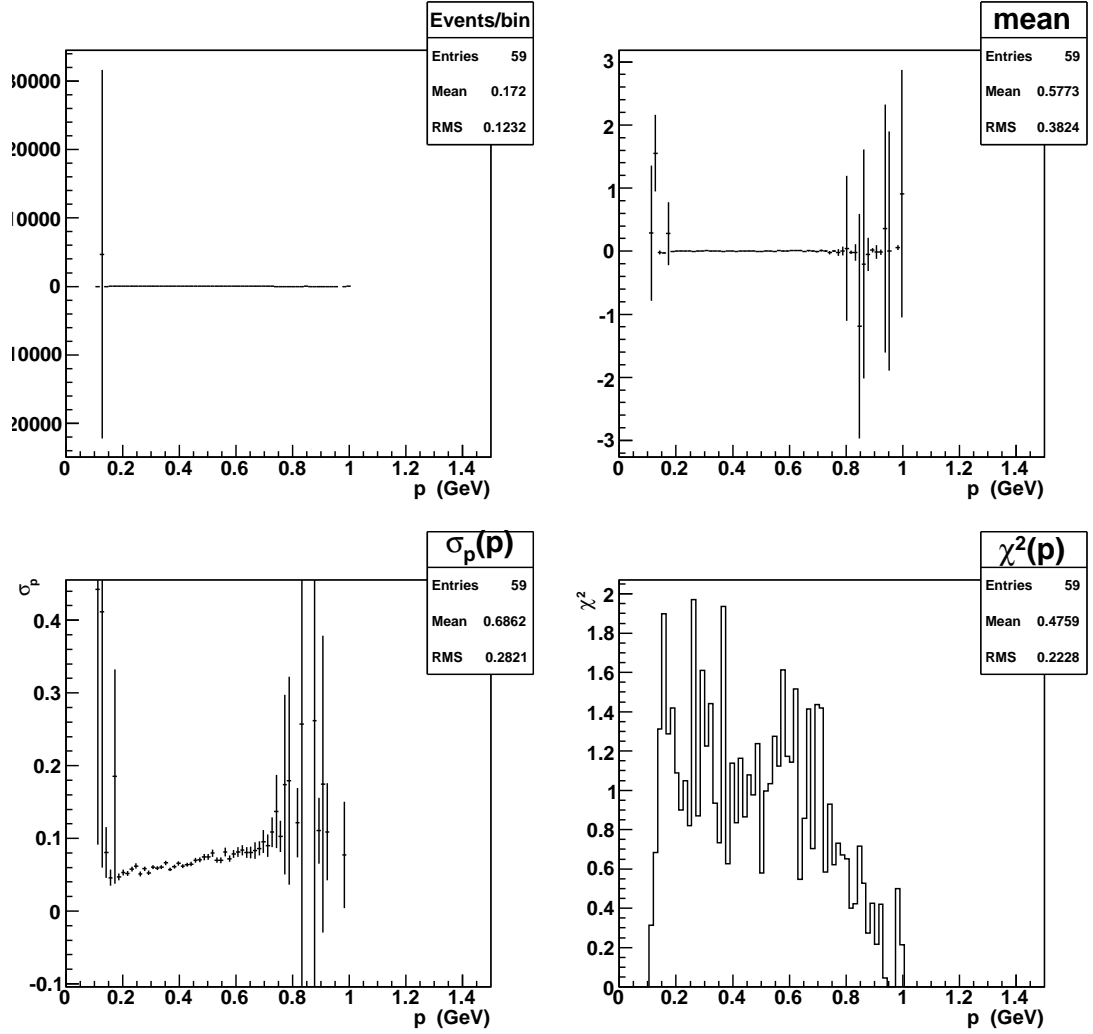
Figure 13: The $g11a$ study of $\sigma_\theta(\theta)$. The upper left plot shows the number of events per bin used. The upper right plot show the mean from the Gaussian fits. The lower left plot shows the values of σ from the Gaussian fits over the required range of θ. The lower right plot shows the χ^2 from each Gaussian fit for every bin used (angular units are radians).
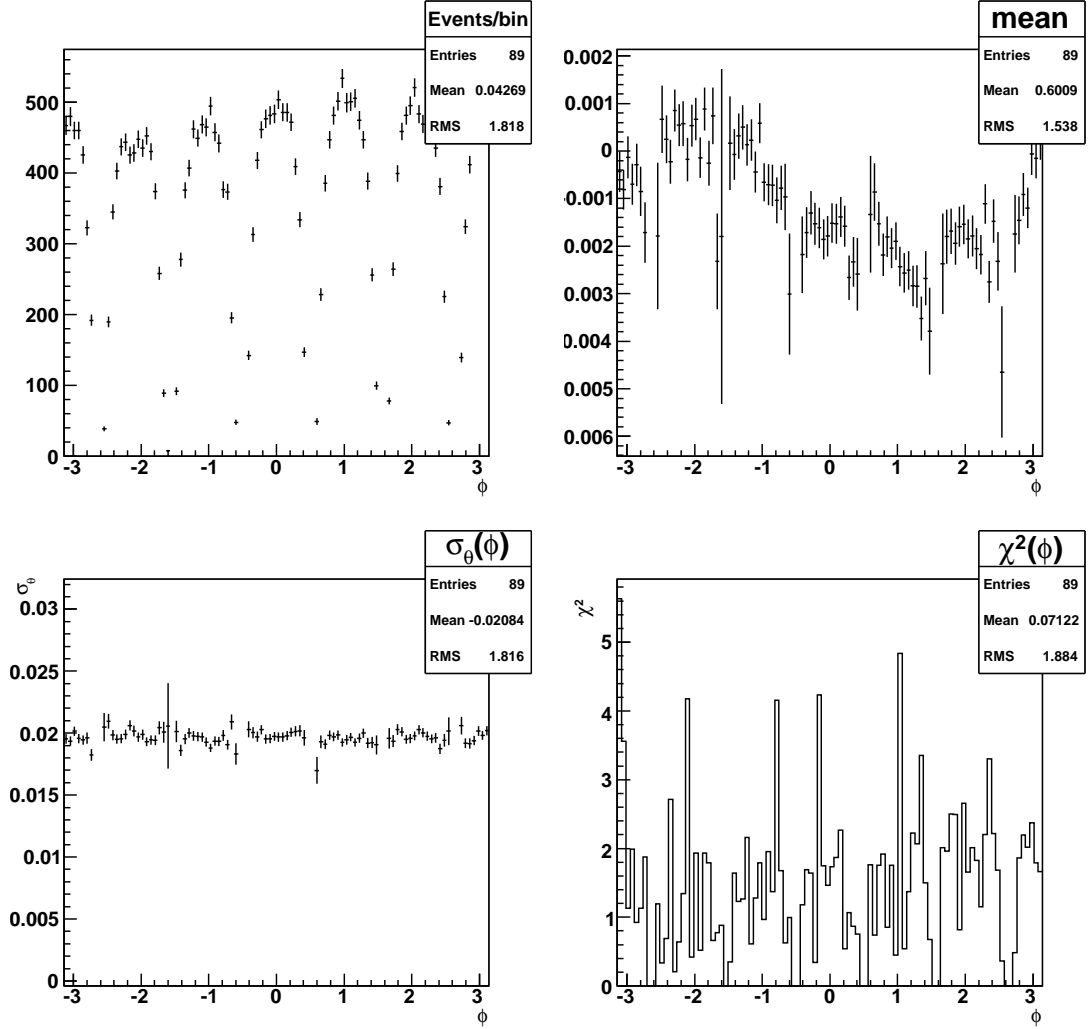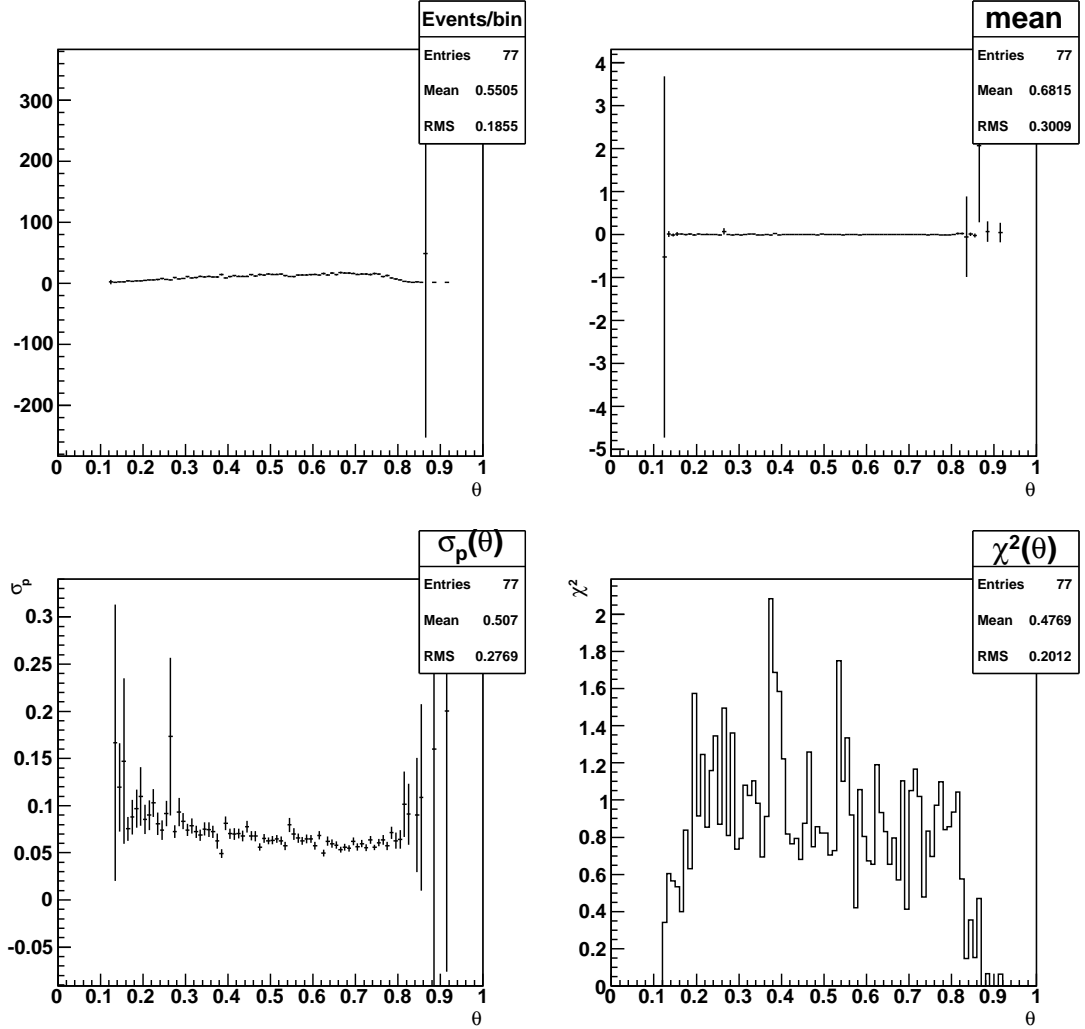
Figure 14: The $g11a$ study of $\sigma_\theta(\phi)$. The upper left plot shows the number of events per bin used. The upper right plot show the mean from the Gaussian fits. The lower left plot shows the values of σ from the Gaussian fits over the required range of ϕ. The lower right plot shows the χ^2 from each Gaussian fit for every bin used (angular units are radians).
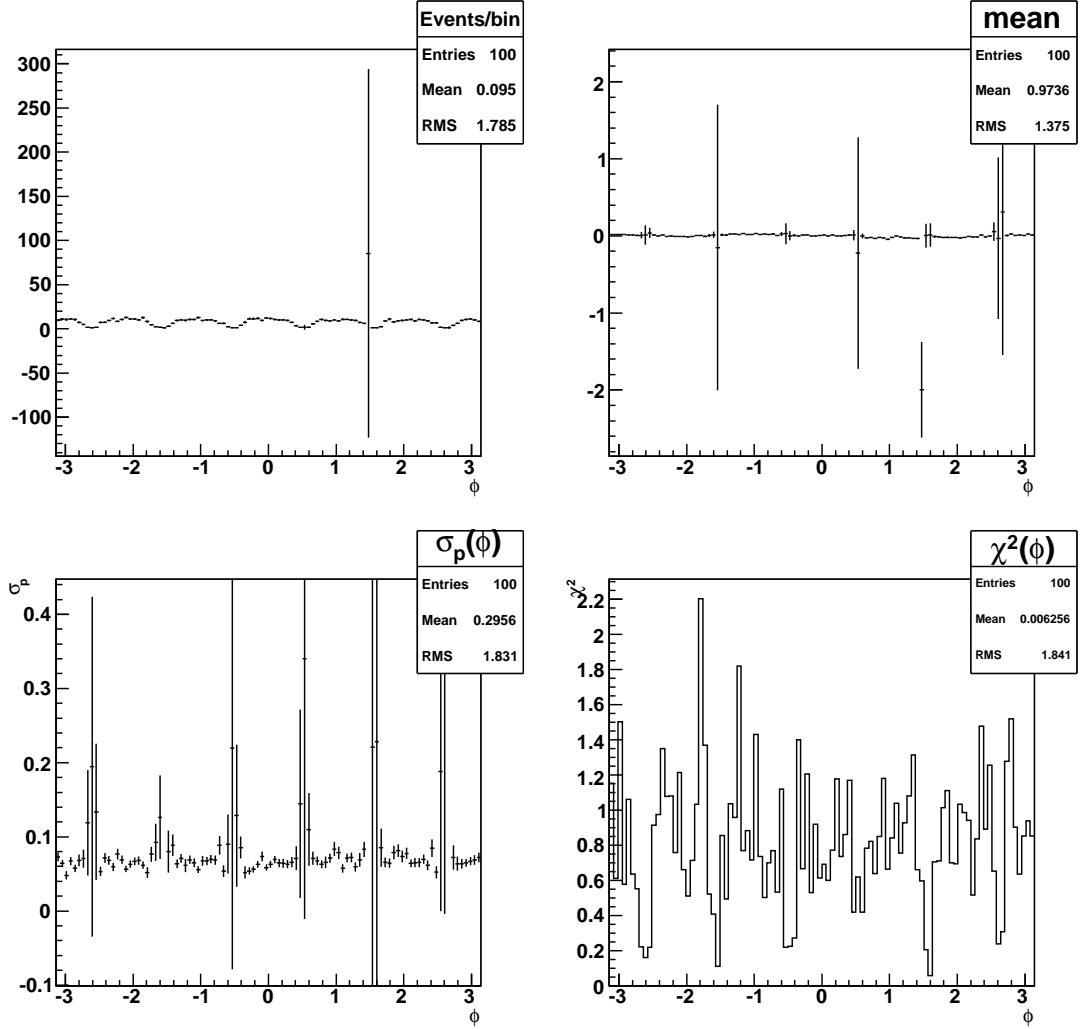
Figure 15: The $g11a$ study of $\sigma_\phi(p)$. The upper left plot shows the number of events per bin used. The upper right plot show the mean from the Gaussian fits. The lower left plot shows the values of σ from the Gaussian fits over the required range of p. The lower right plot shows the χ^2 from each Gaussian fit for every bin used (angular units are radians).
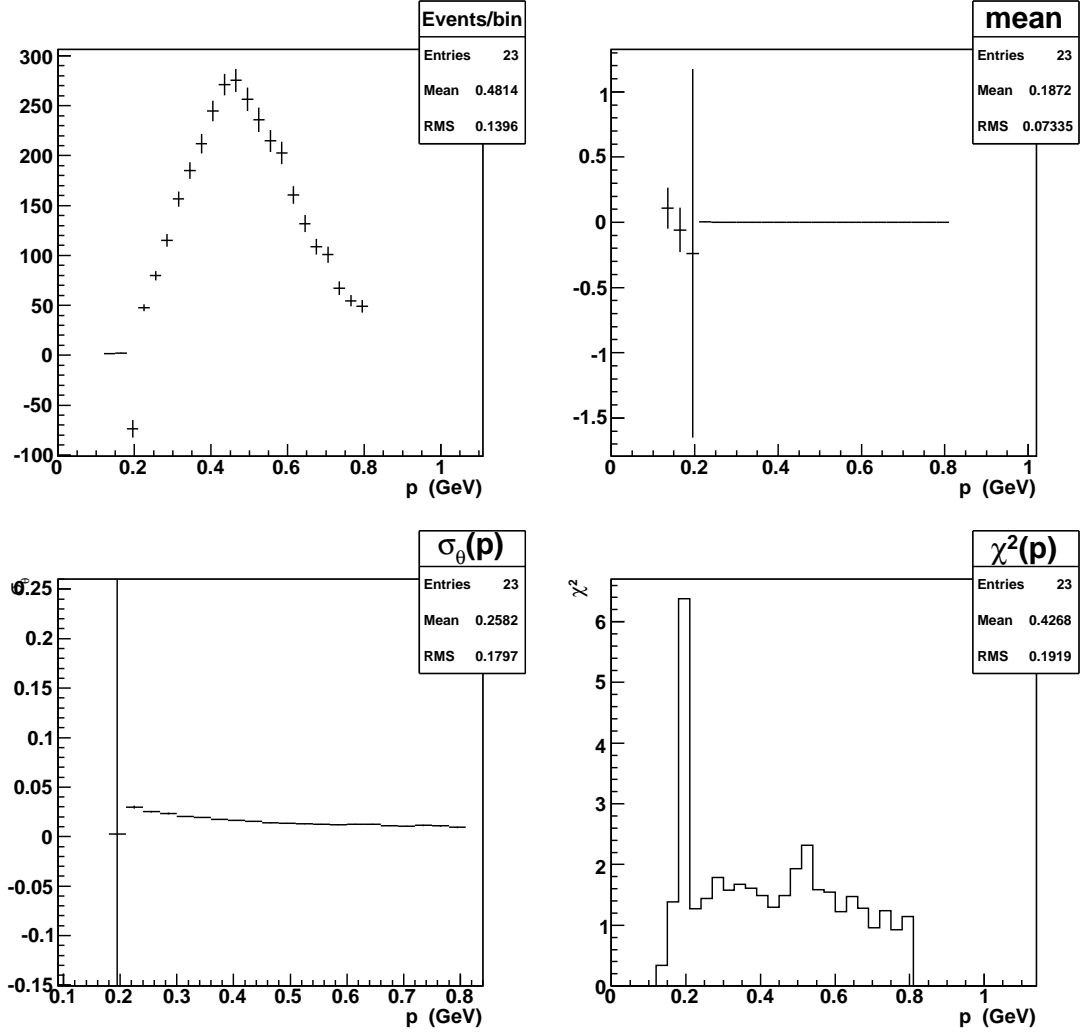
Figure 16: The $g11a$ study of $\sigma_\phi(\theta)$. The upper left plot shows the number of events per bin used. The upper right plot show the mean from the Gaussian fits. The lower left plot shows the values of σ from the Gaussian fits over the required range of θ. The lower right plot shows the χ^2 from each Gaussian fit for every bin used (angular units are radians).

Figure 17: The $g11a$ study of $\sigma_\phi(\phi)$. The upper left plot shows the number of events per bin used. The upper right plot show the mean from the Gaussian fits. The lower left plot shows the values of σ from the Gaussian fits over the required range of ϕ. The lower right plot shows the χ^2 from each Gaussian fit for every bin used (angular units are radians).
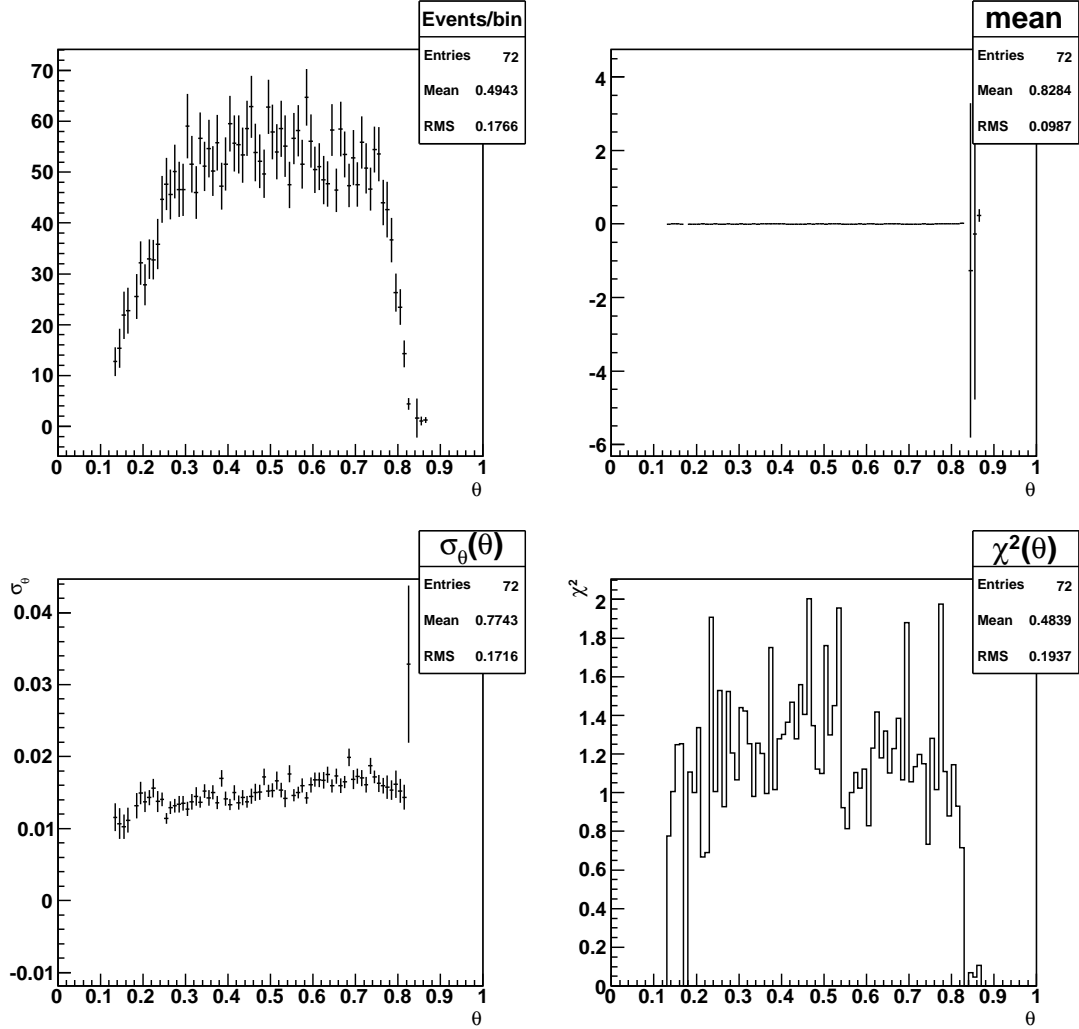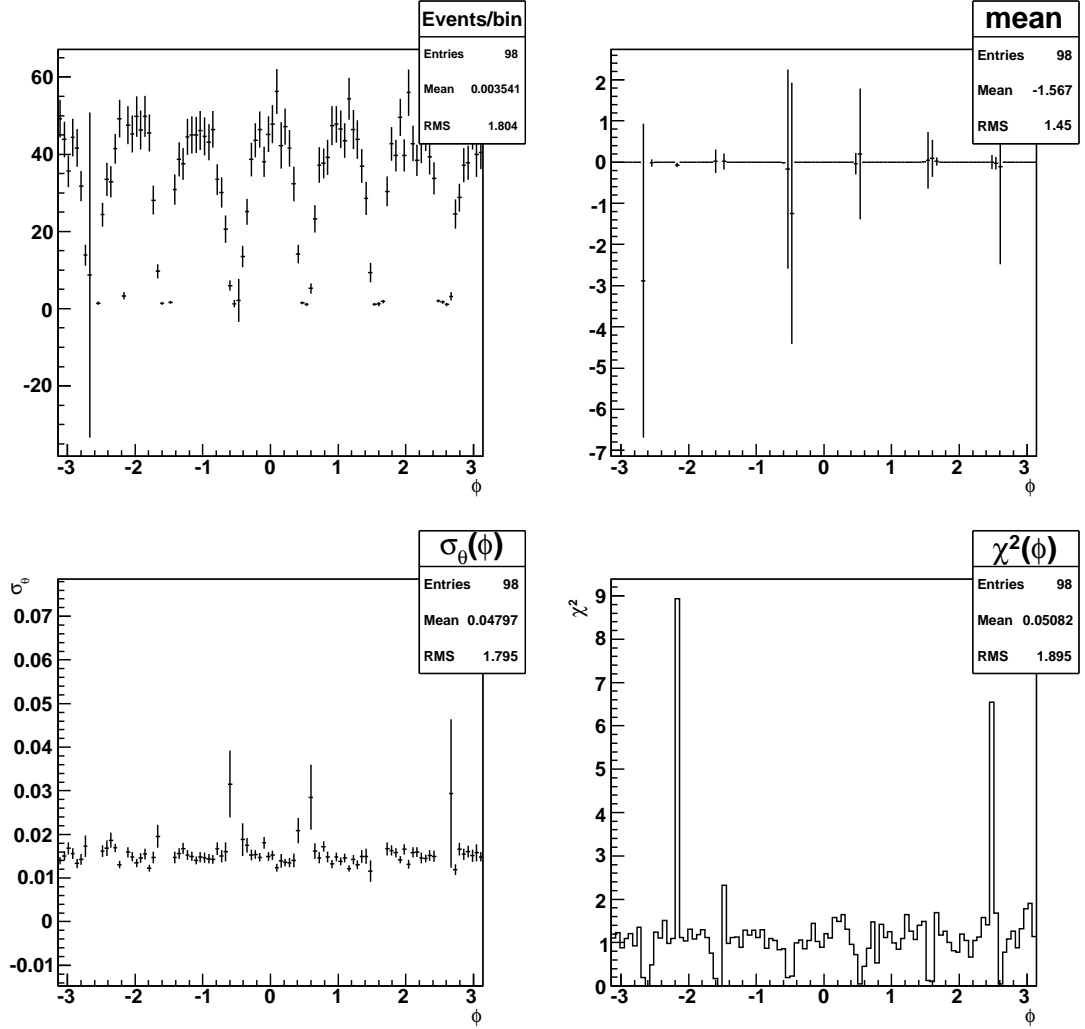
Figure 18: The Monte Carlo study of $\sigma_p(p)$. The upper left plot shows the number of events per bin used. The upper right plot show the mean from the Gaussian fits. The lower left plot shows the values of σ from the Gaussian fits over the required range of p. The lower right plot shows the χ^2 from each Gaussian fit for every bin used.

Figure 19: The Monte Carlo study of $\sigma_p(\theta)$. The upper left plot shows the number of events per bin used. The upper right plot show the mean from the Gaussian fits. The lower left plot shows the values of σ from the Gaussian fits over the required range of θ. The lower right plot shows the χ^2 from each Gaussian fit for every bin used (angular units are radians).
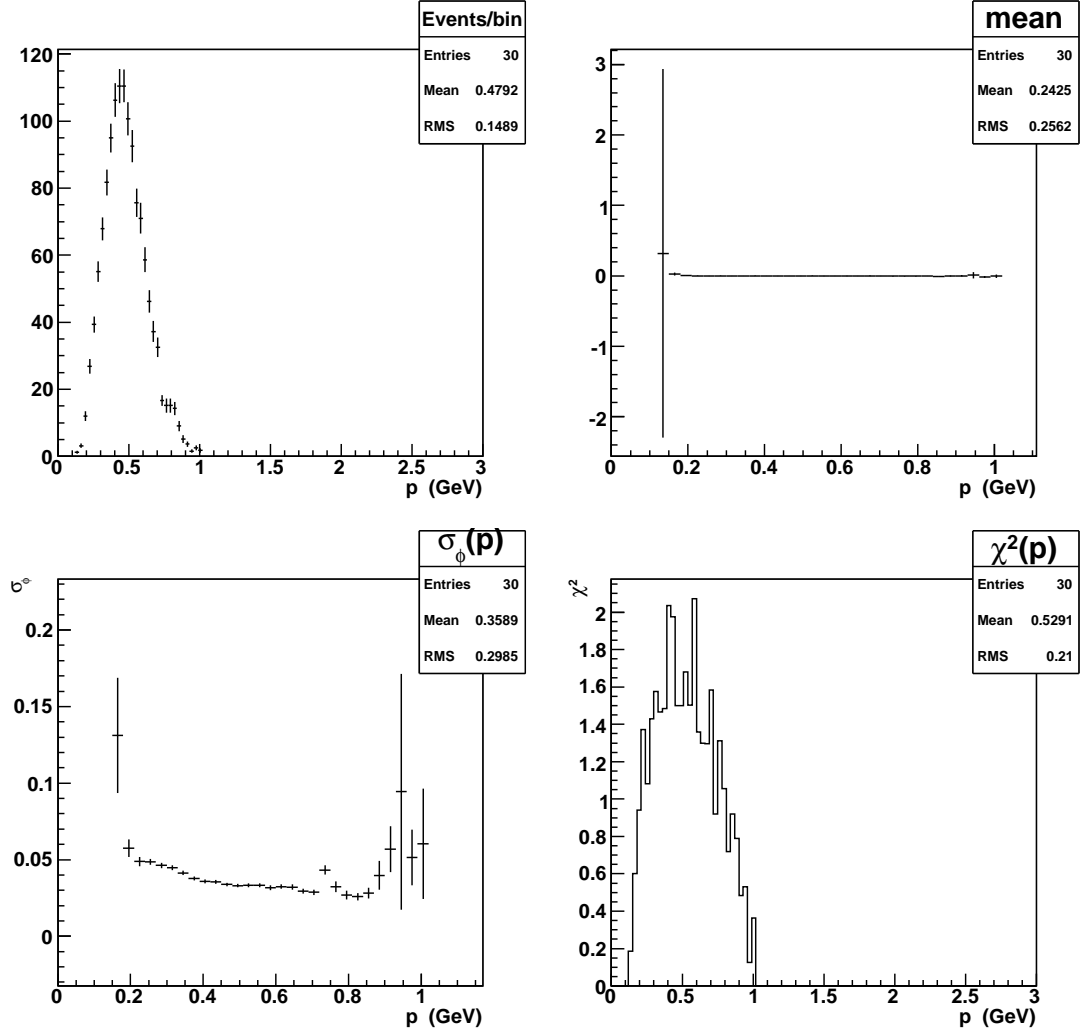
Figure 20: The Monte Carlo study of $\sigma_p(\phi)$. The upper left plot shows the number of events per bin used. The upper right plot show the mean from the Gaussian fits. The lower left plot shows the values of σ from the Gaussian fits over the required range of ϕ. The lower right plot shows the χ^2 from each Gaussian fit for every bin used (angular units are radians).
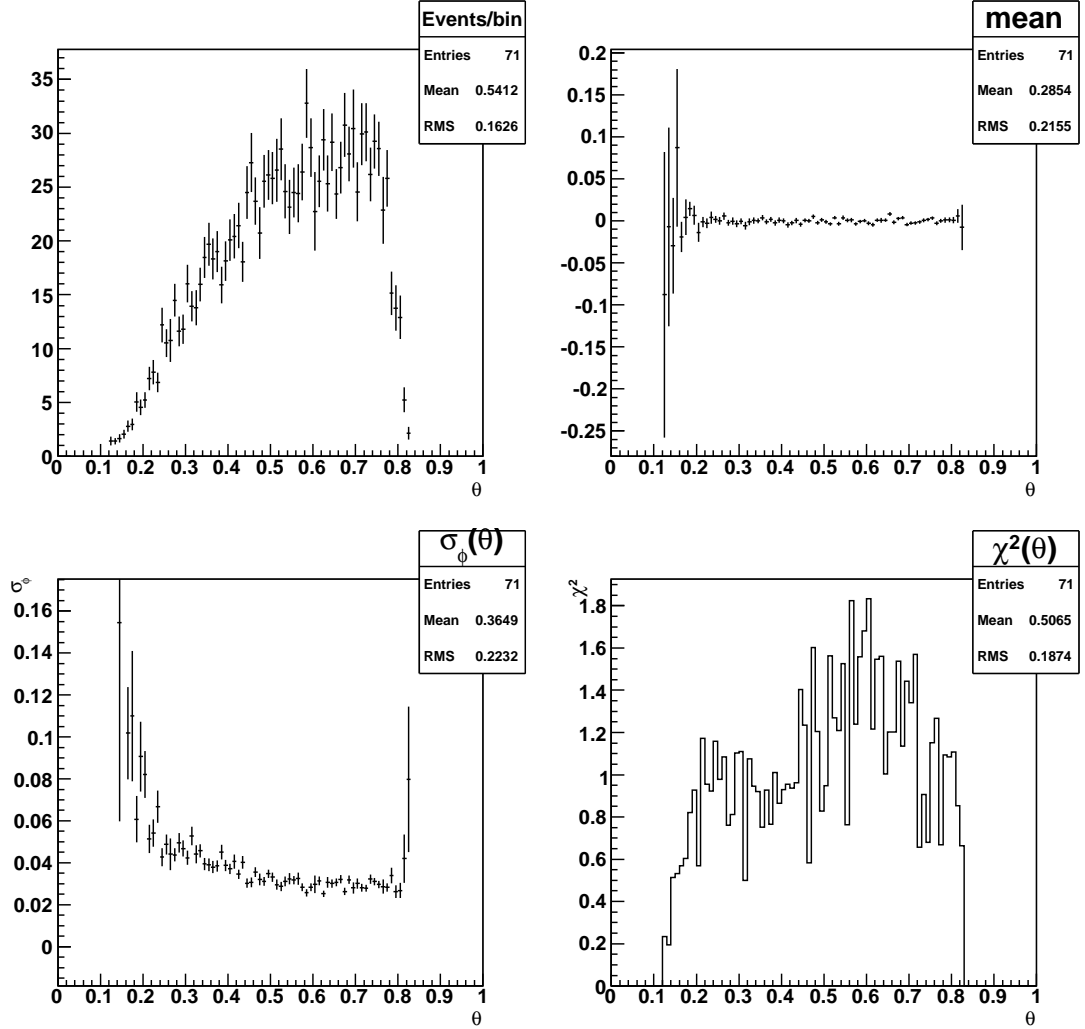
Figure 21: The Monte Carlo study of $\sigma_\theta(p)$. The upper left plot shows the number of events per bin used. The upper right plot show the mean from the Gaussian fits. The lower left plot shows the values of σ from the Gaussian fits over the required range of p. The lower right plot shows the χ^2 from each Gaussian fit for every bin used (angular units are radians).
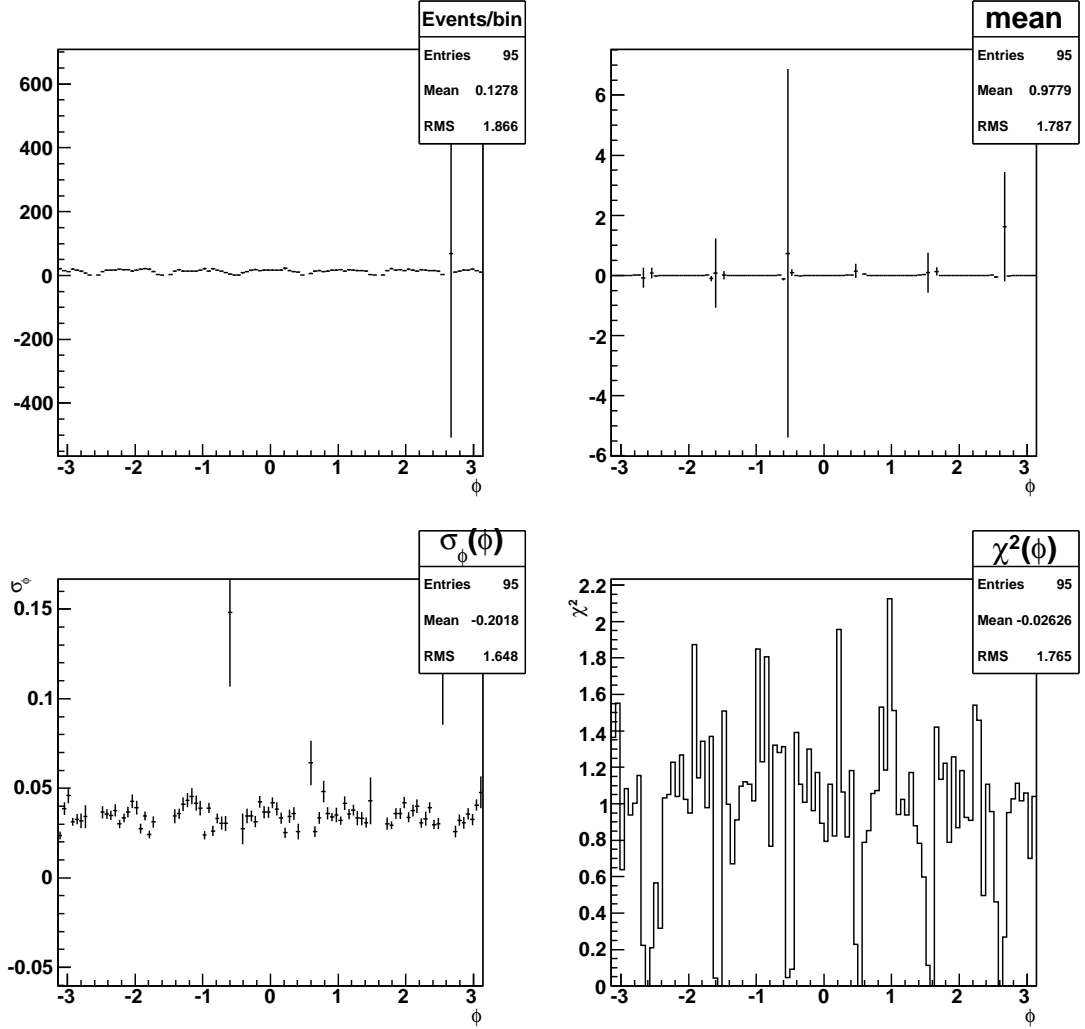
Figure 22: The Monte Carlo study of $\sigma_\theta(\theta)$. The upper left plot shows the number of events per bin used. The upper right plot show the mean from the Gaussian fits. The lower left plot shows the values of σ from the Gaussian fits over the required range of θ. The lower right plot shows the χ^2 from each Gaussian fit for every bin used (angular units are radians).

Figure 23: The Monte Carlo study of $\sigma_\theta(\phi)$. The upper left plot shows the number of events per bin used. The upper right plot show the mean from the Gaussian fits. The lower left plot shows the values of σ from the Gaussian fits over the required range of ϕ. The lower right plot shows the χ^2 from each Gaussian fit for every bin used (angular units are radians).

Figure 24: The Monte Carlo study of $\sigma_\phi(p)$. The upper left plot shows the number of events per bin used. The upper right plot show the mean from the Gaussian fits. The lower left plot shows the values of σ from the Gaussian fits over the required range of p. The lower right plot shows the χ^2 from each Gaussian fit for every bin used (angular units are radians).

Figure 25: The Monte Carlo study of $\sigma_\phi(\theta)$. The upper left plot shows the number of events per bin used. The upper right plot show the mean from the Gaussian fits. The lower left plot shows the values of σ from the Gaussian fits over the required range of θ. The lower right plot shows the χ^2 from each Gaussian fit for every bin used (angular units are radians).

Figure 26: The Monte Carlo study of $\sigma_\phi(\phi)$. The upper left plot shows the number of events per bin used. The upper right plot show the mean from the Gaussian fits. The lower left plot shows the values of σ from the Gaussian fits over the required range of ϕ. The lower right plot shows the χ^2 from each Gaussian fit for every bin used (angular units are radians).
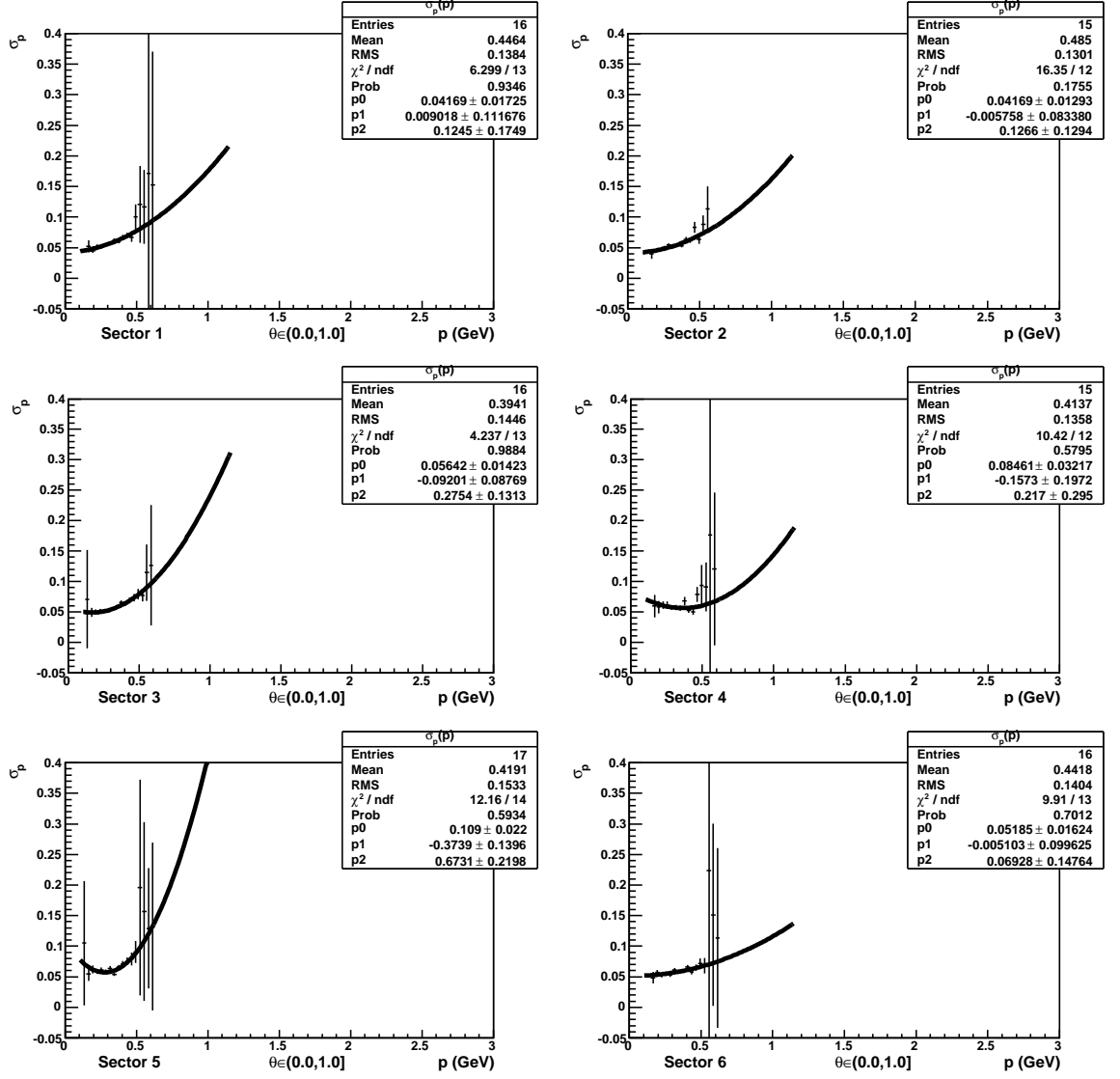
Figure 27: The $g11a$ momentum resolution σ_p for each CLAS EC sector for $\theta\epsilon(0.0, 1.0]$ with a quadratic fit over the momentum range of 0.1-1.15 GeV.
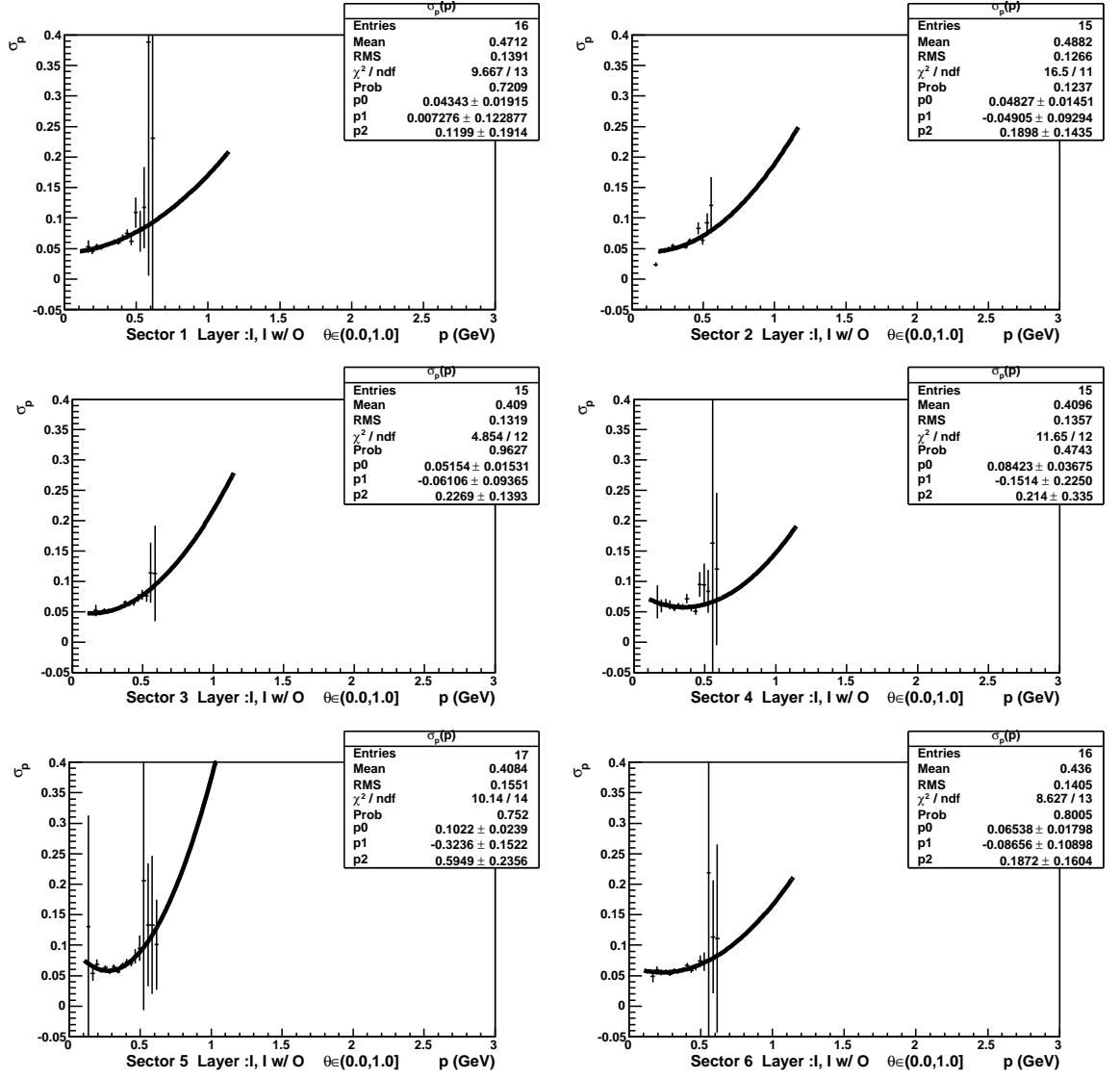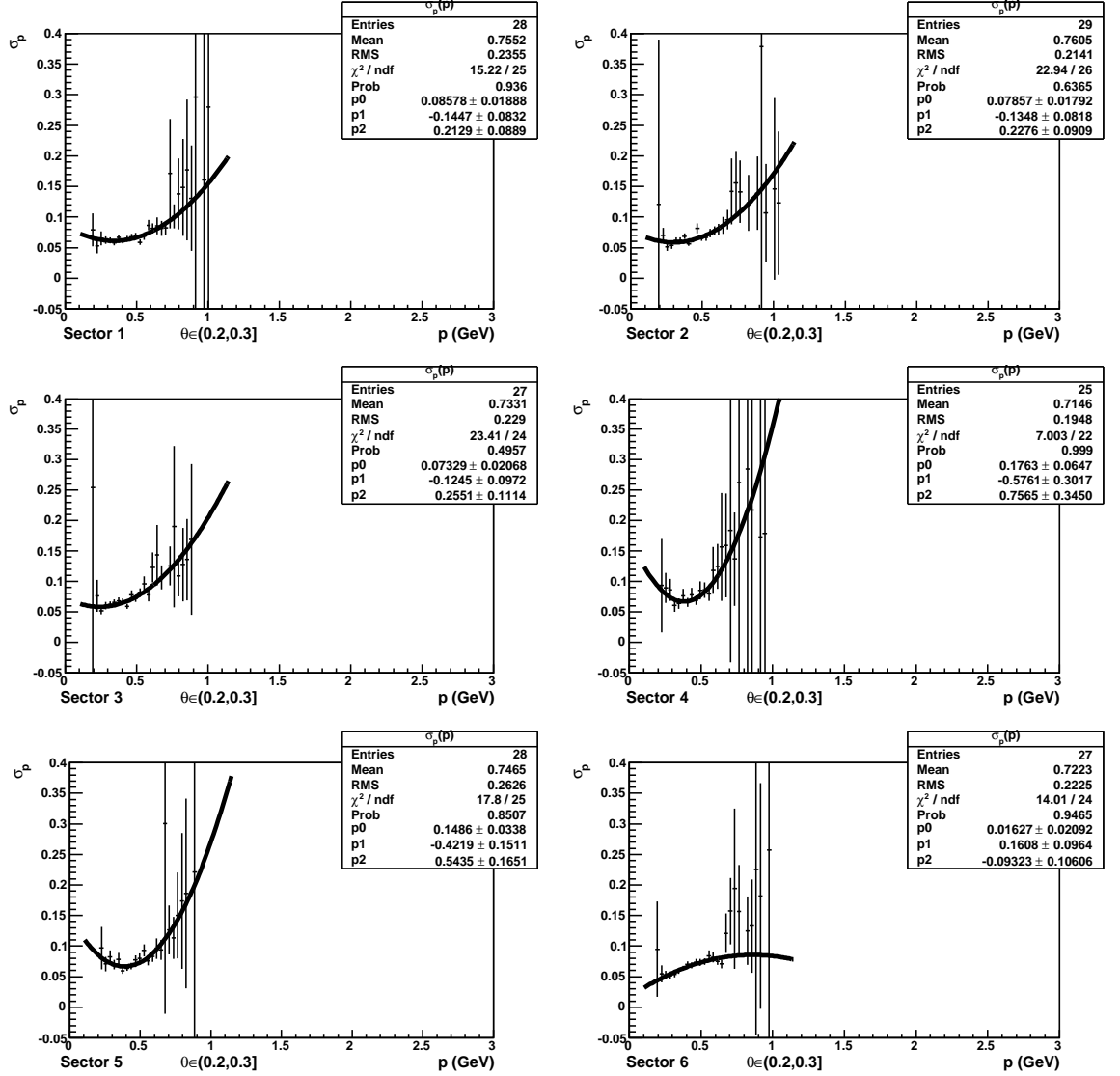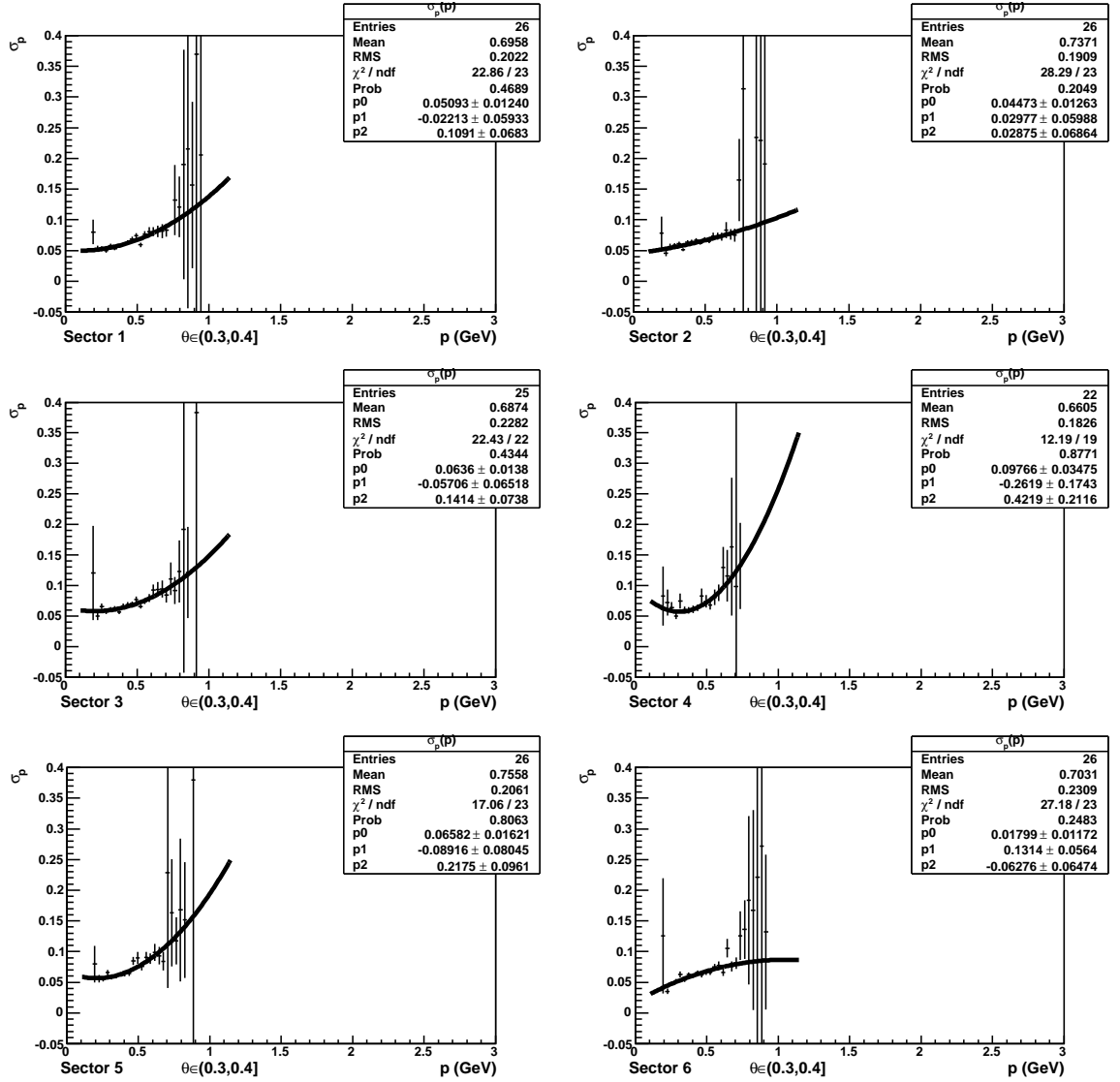
Figure 28: The $g11a$ momentum resolution σ_p for each CLAS EC sector for $\theta\epsilon(0.0, 1.0]$ with a quadratic fit over the momentum range of 0.1-1.15 GeV using EC hits from the inner or inner with outer block.
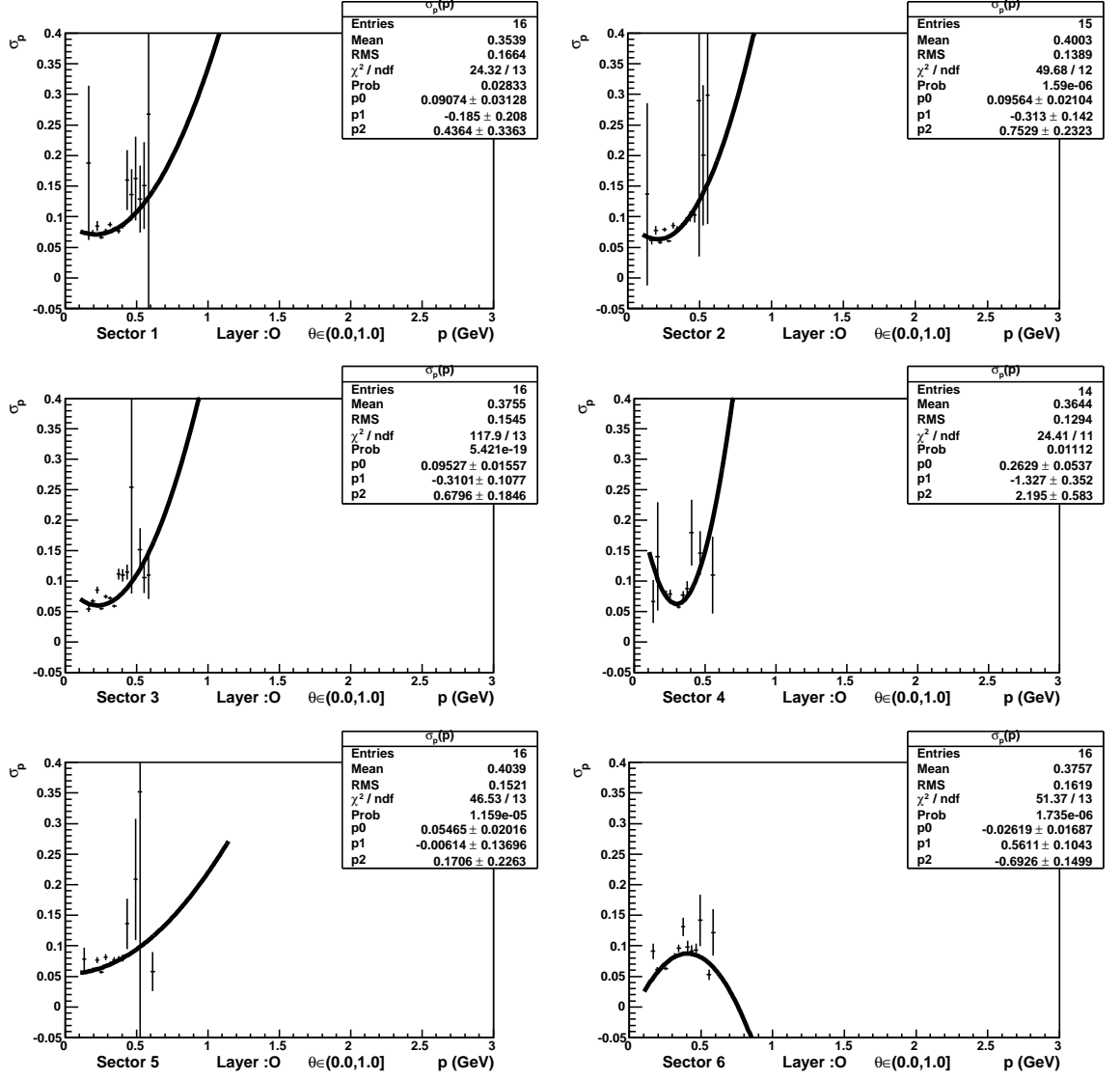
Figure 29: The $g11a$ momentum resolution σ_p for each CLAS EC sector for $\theta\epsilon(0.0, 1.0]$ with a quadratic fit over the momentum range of 0.1-1.15 GeV using EC hits from the outer block only.
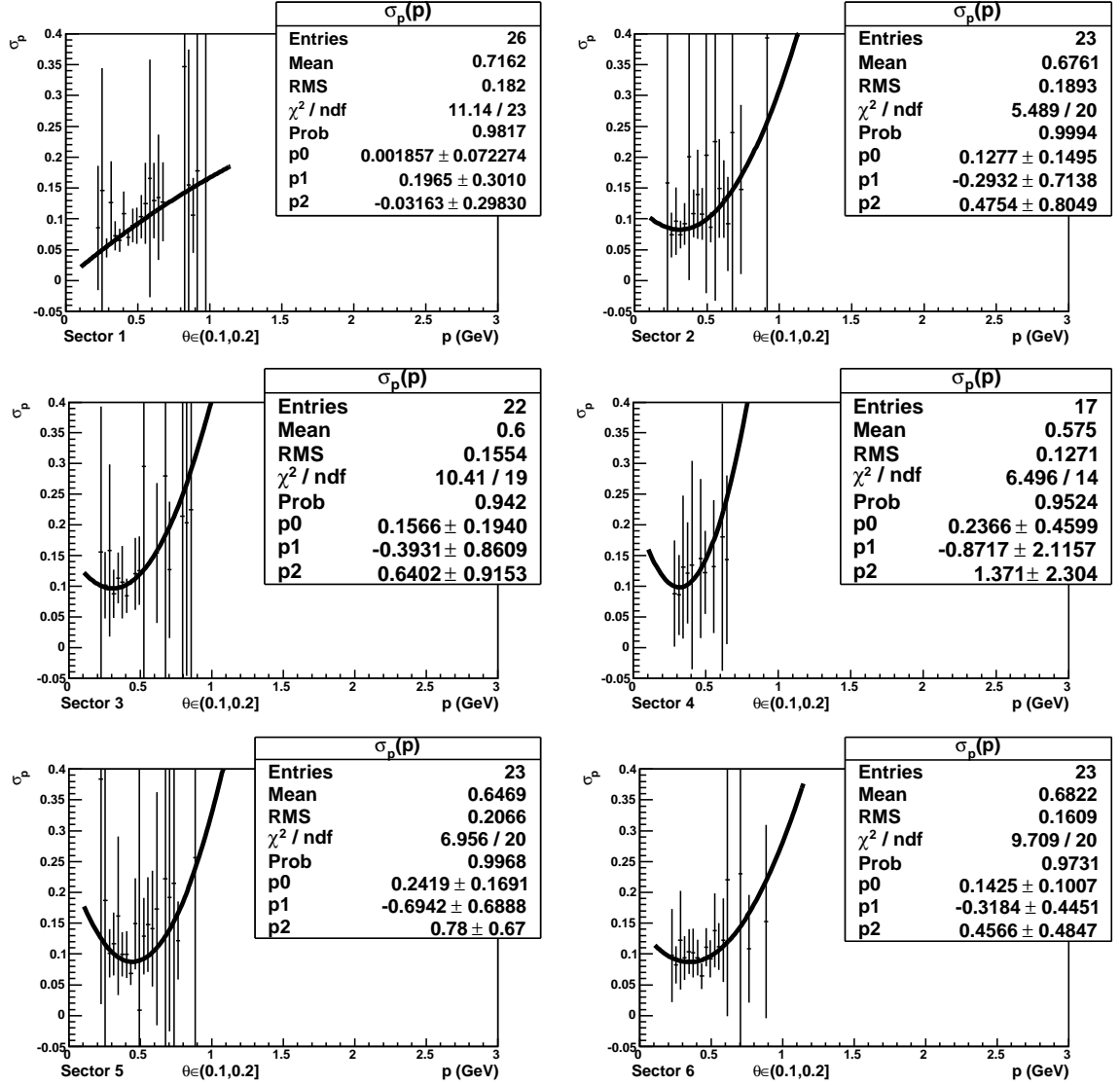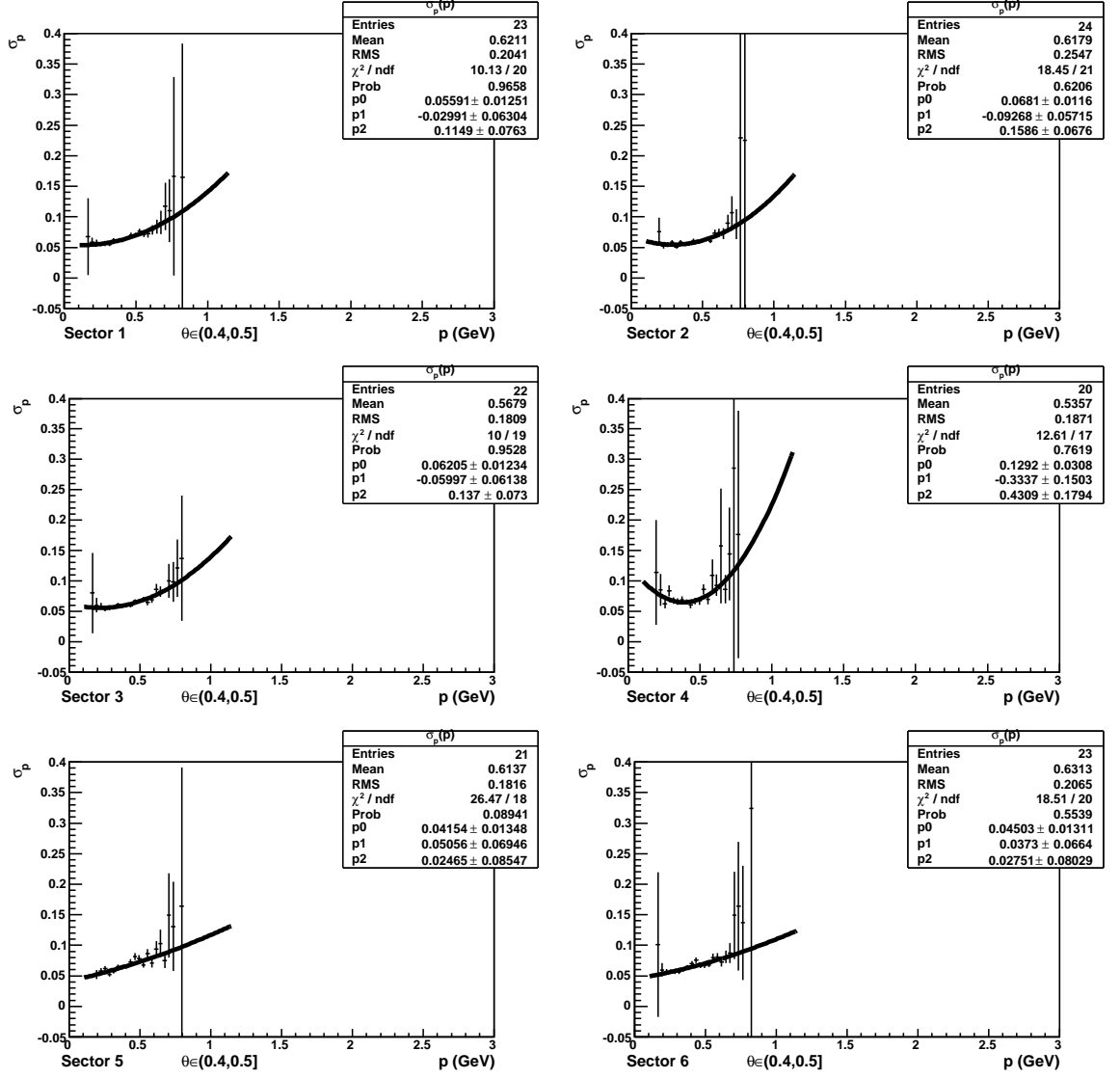
Figure 30: The $g11a$ momentum resolution σ_p for each CLAS EC sector for $\theta\epsilon(0.1, 0.2]$ with a quadratic fit over the momentum range of 0.1-1.15 GeV.
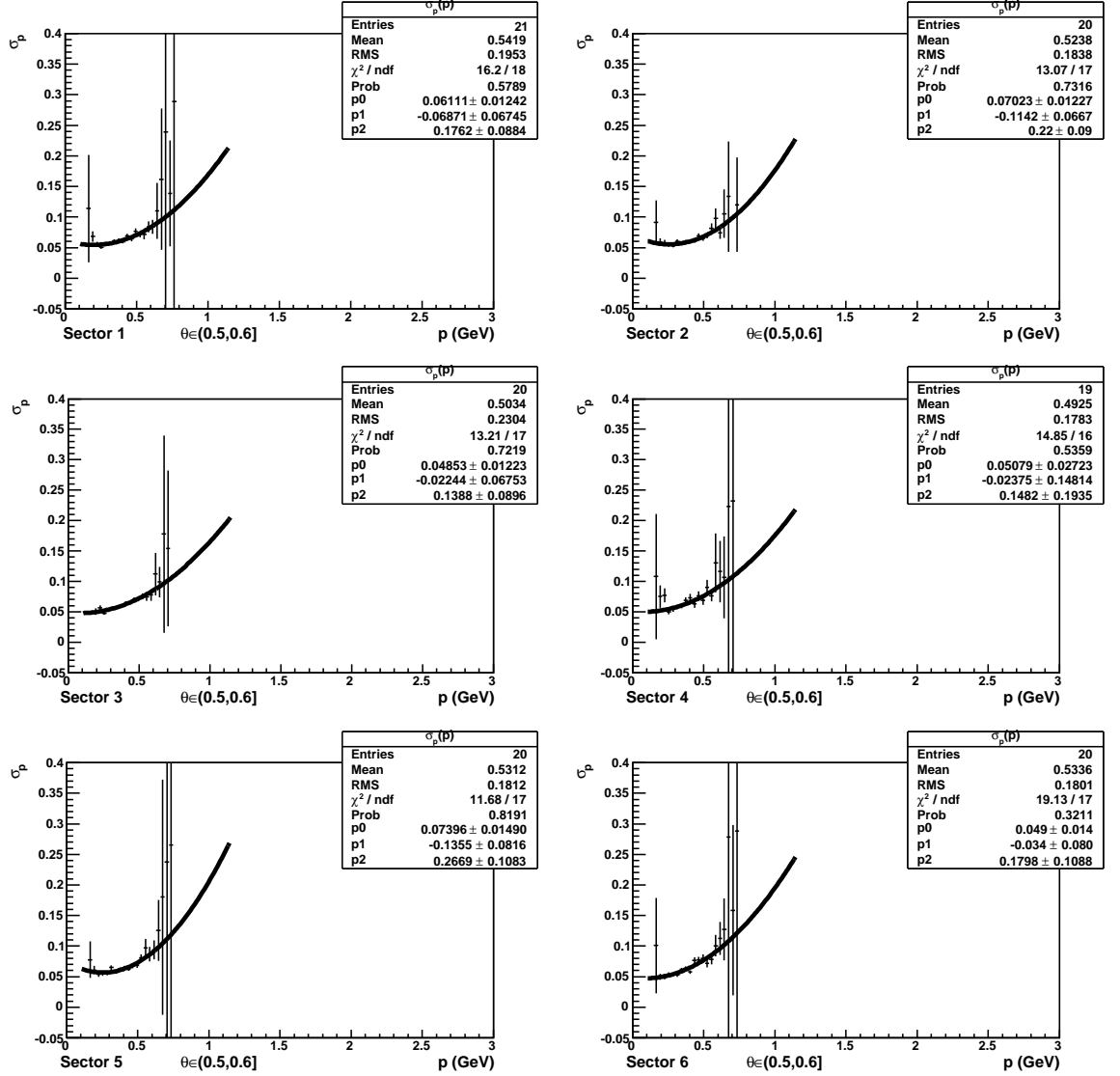
Figure 31: The $g11a$ momentum resolution σ_p for each CLAS EC sector for $\theta\epsilon(0.2, 0.3]$ with a quadratic fit over the momentum range of 0.1-1.15 GeV.
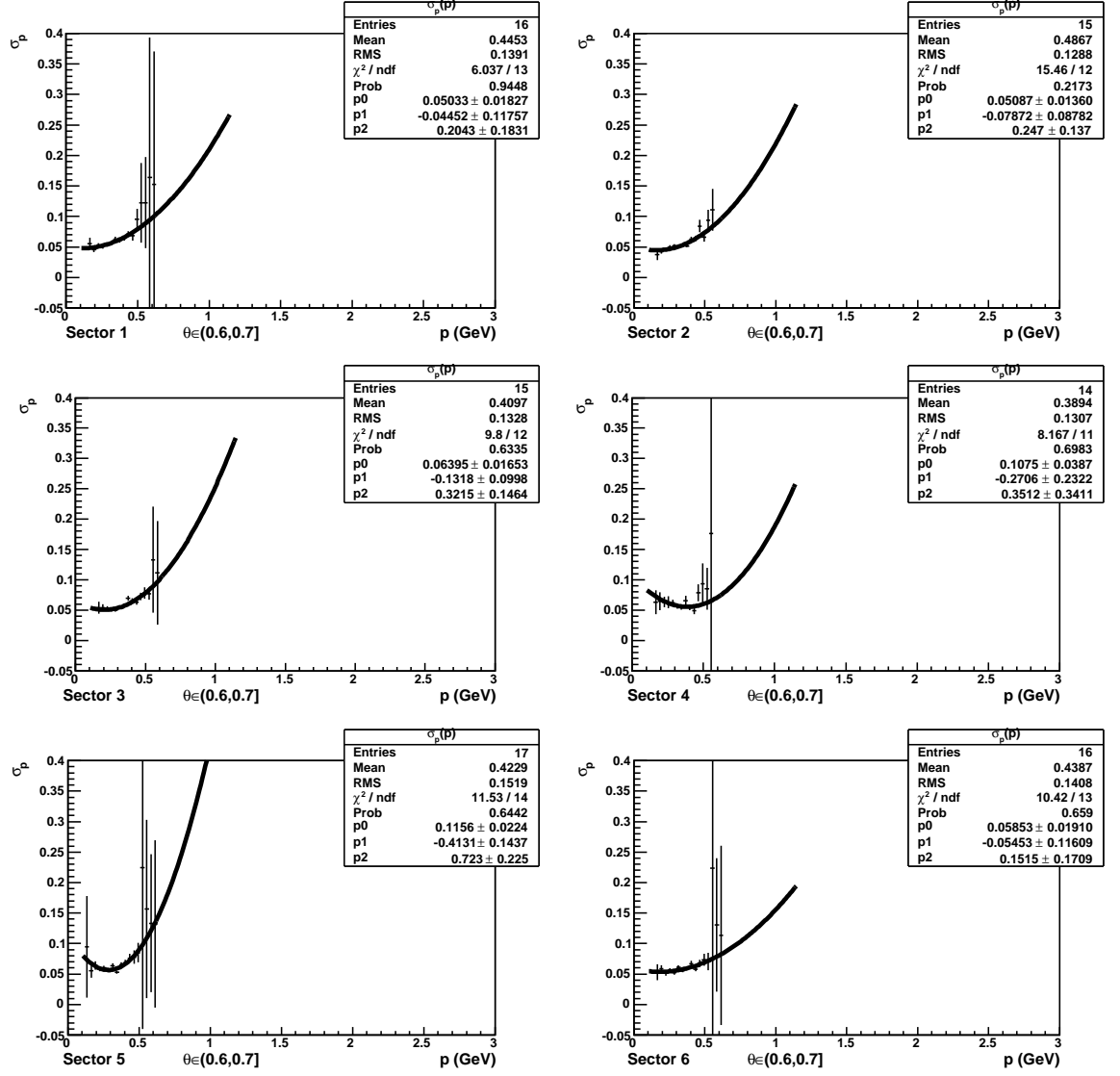
Figure 32: The $g11a$ momentum resolution σ_p for each CLAS EC sector for $\theta\epsilon(0.3, 0.4]$ with a quadratic fit over the momentum range of 0.1-1.15 GeV.

Figure 33: The $g11a$ momentum resolution σ_p for each CLAS EC sector for $\theta\epsilon(0.4, 0.5]$ with a quadratic fit over the momentum range of 0.1-1.15 GeV.
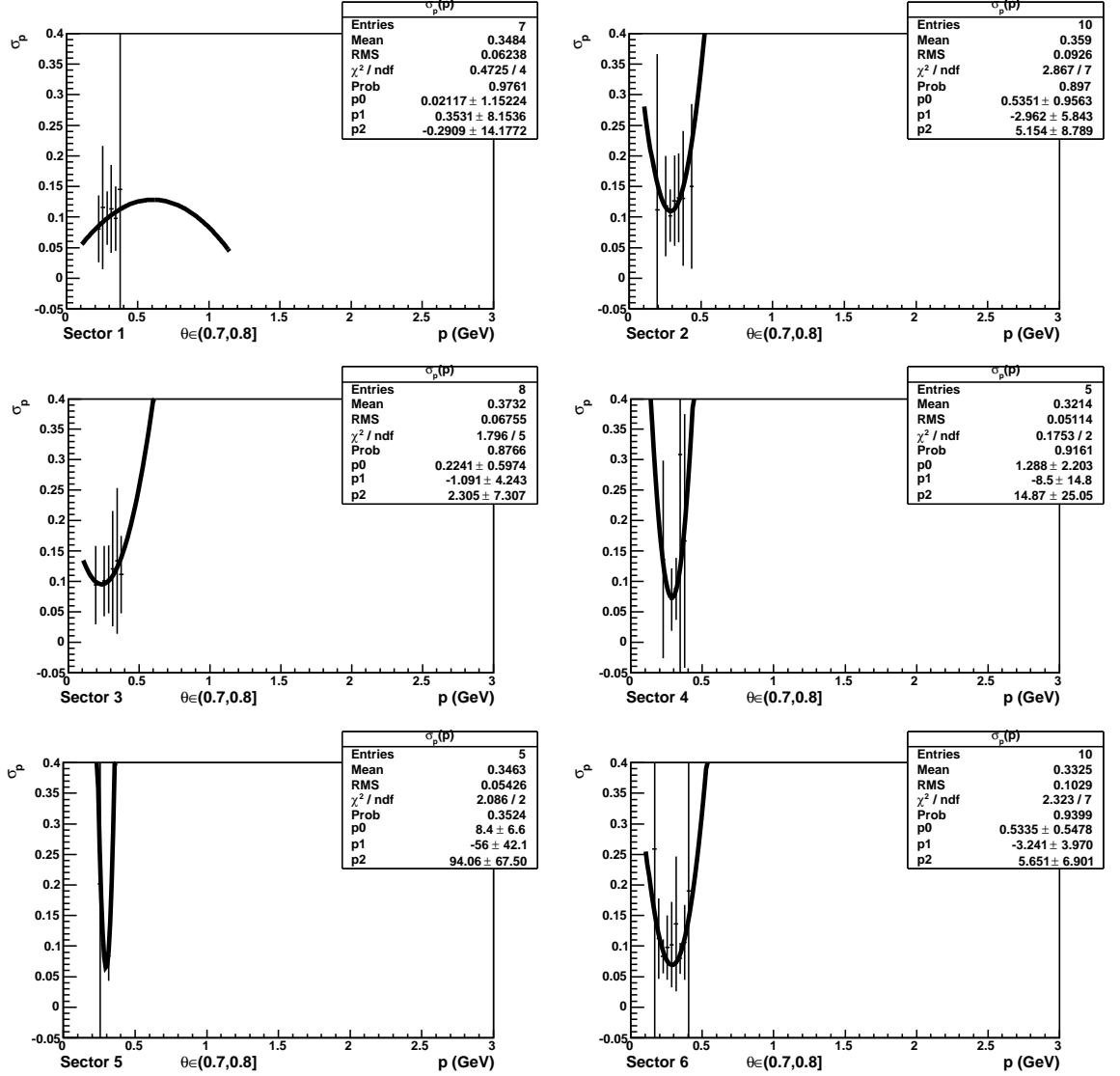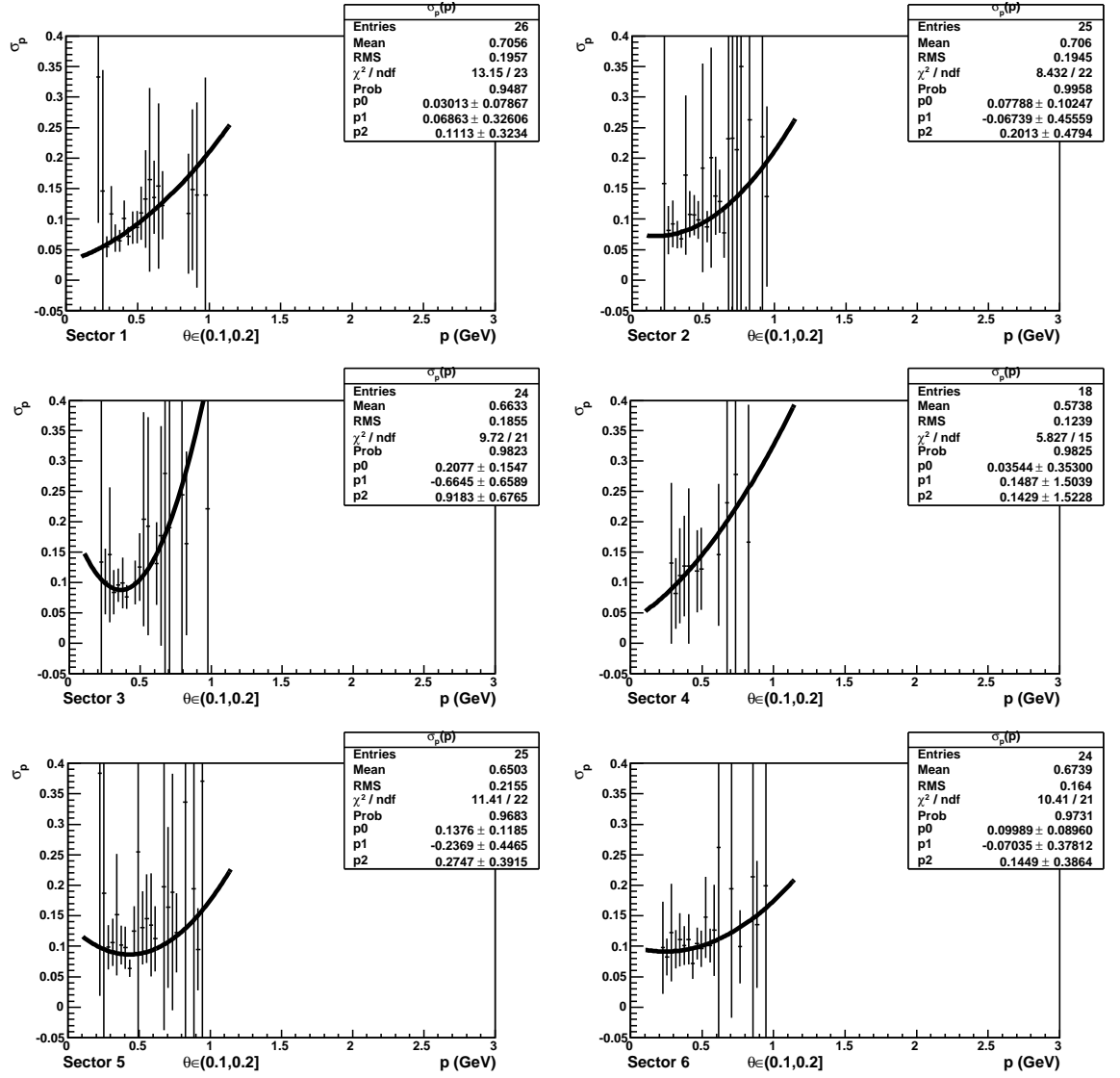
Figure 34: The $g11a$ momentum resolution σ_p for each CLAS EC sector for $\theta\epsilon(0.5, 0.6]$ with a quadratic fit over the momentum range of 0.1-1.15 GeV.

Figure 35: The $g11a$ momentum resolution σ_p for each CLAS EC sector for $\theta\epsilon(0.6, 0.7]$ with a quadratic fit over the momentum range of 0.1-1.15 GeV.

Figure 36: The $g11a$ momentum resolution σ_p for each CLAS EC sector for $\theta\epsilon(0.7, 0.8]$ with a quadratic fit over the momentum range of 0.1-1.15 GeV.

Figure 37: The Monte Carlo momentum resolution σ_p for each CLAS EC sector for $\theta\epsilon(0.1, 0.2]$ with a quadratic fit over the momentum range of 0.1-1.15 GeV.
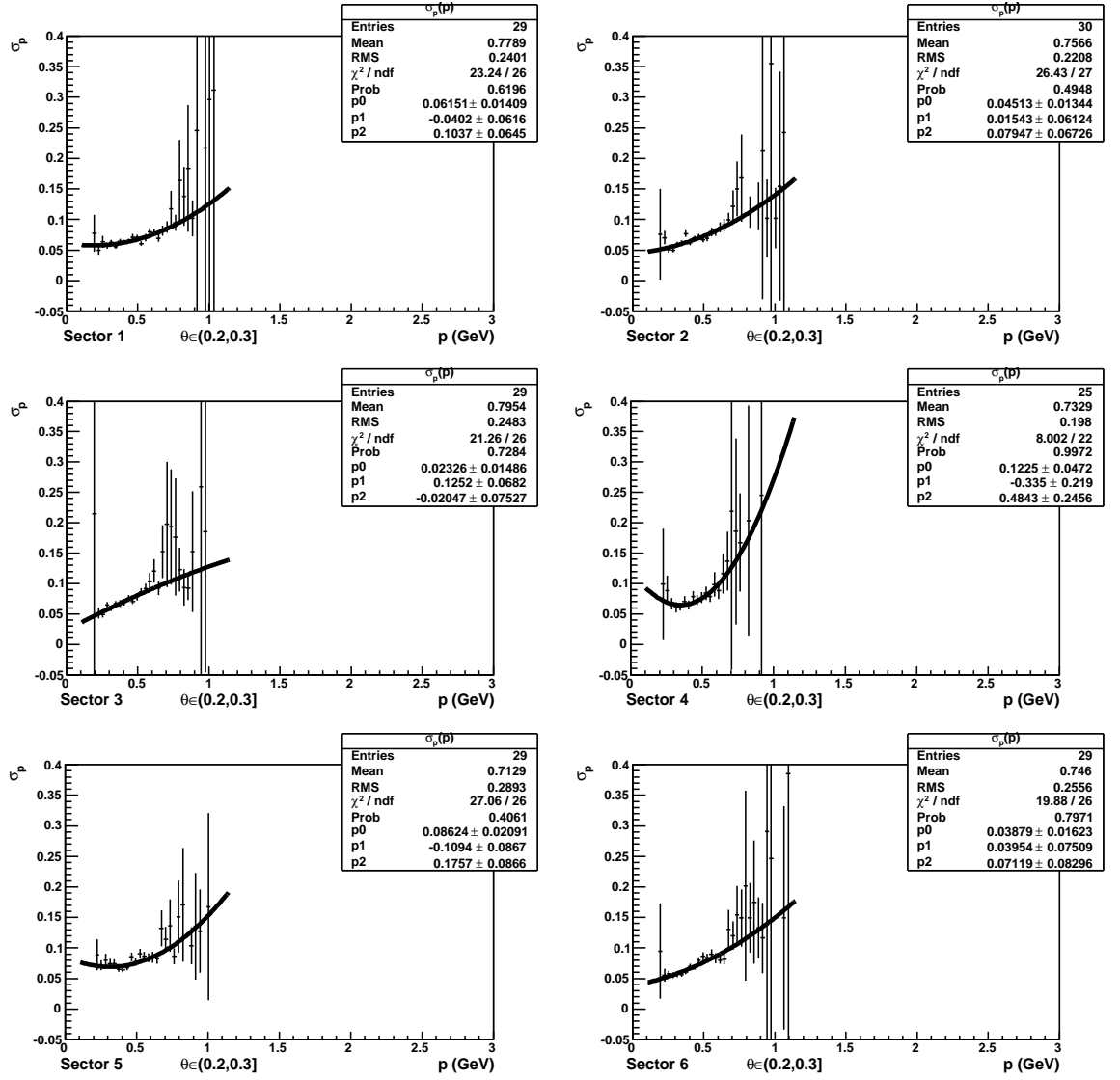
Figure 38: The Monte Carlo momentum resolution σ_p for each CLAS EC sector for $\theta\epsilon(0.2, 0.3]$ with a quadratic fit over the momentum range of 0.1-1.15 GeV.
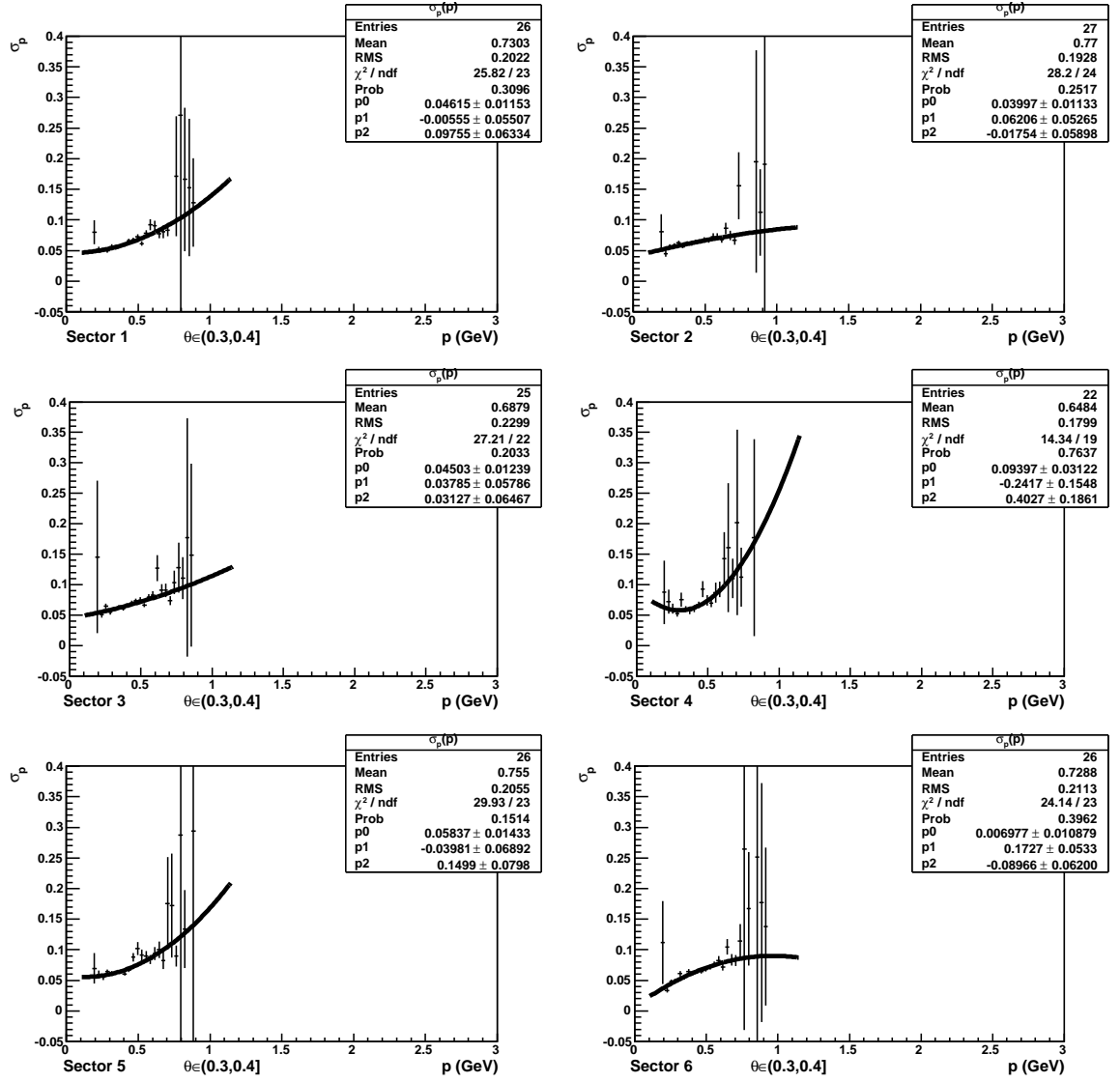
Figure 39: The Monte Carlo momentum resolution σ_p for each CLAS EC sector for $\theta \epsilon (0.3, 0.4]$ with a quadratic fit over the momentum range of 0.1-1.15 GeV.
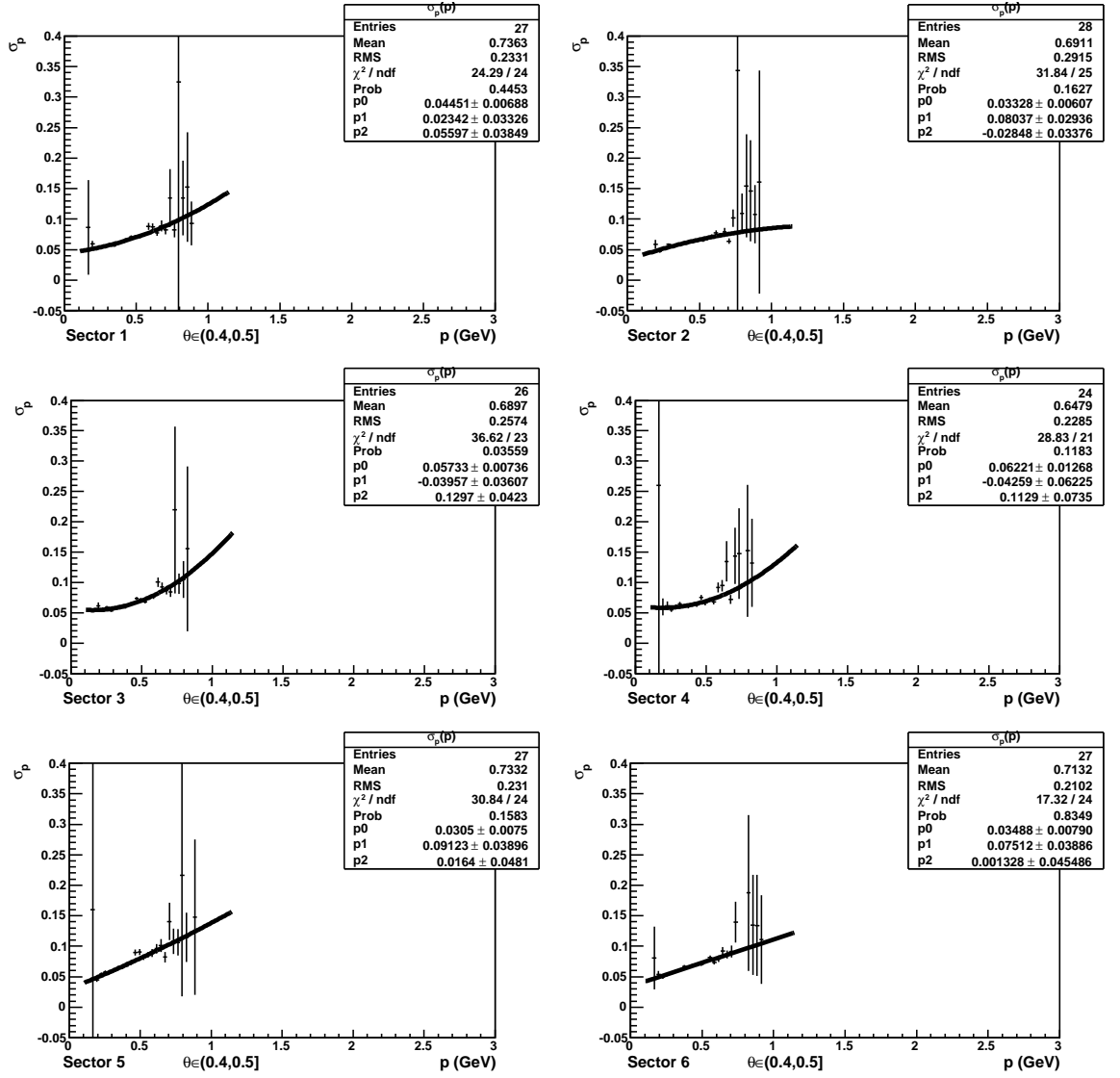
Figure 40: The Monte Carlo momentum resolution σ_p for each CLAS EC sector for $\theta \epsilon (0.4, 0.5]$ with a quadratic fit over the momentum range of 0.1-1.15 GeV.
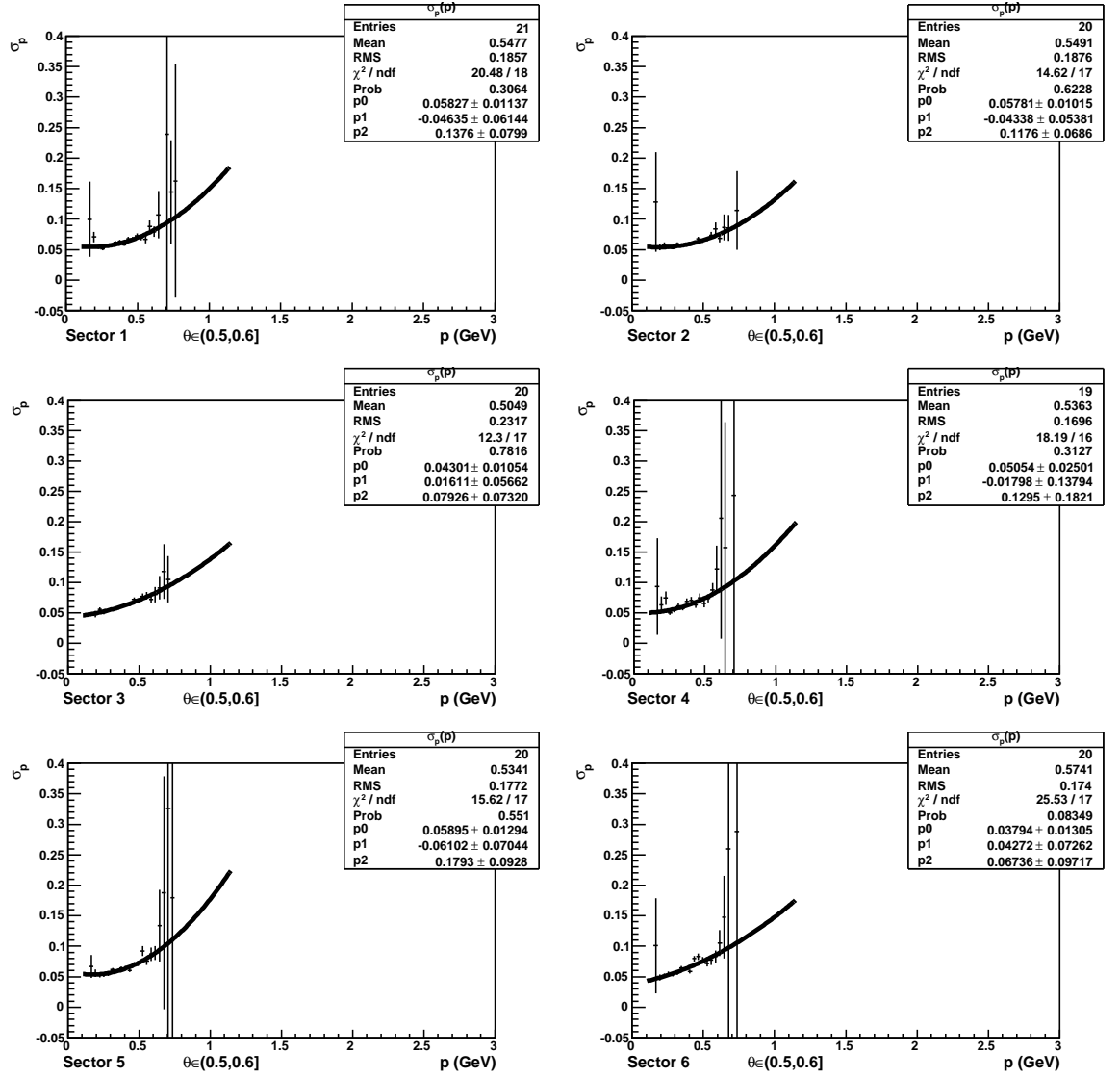
Figure 41: The Monte Carlo momentum resolution σ_p for each CLAS EC sector for $\theta\epsilon(0.5, 0.6]$ with a quadratic fit over the momentum range of 0.1-1.15 GeV.
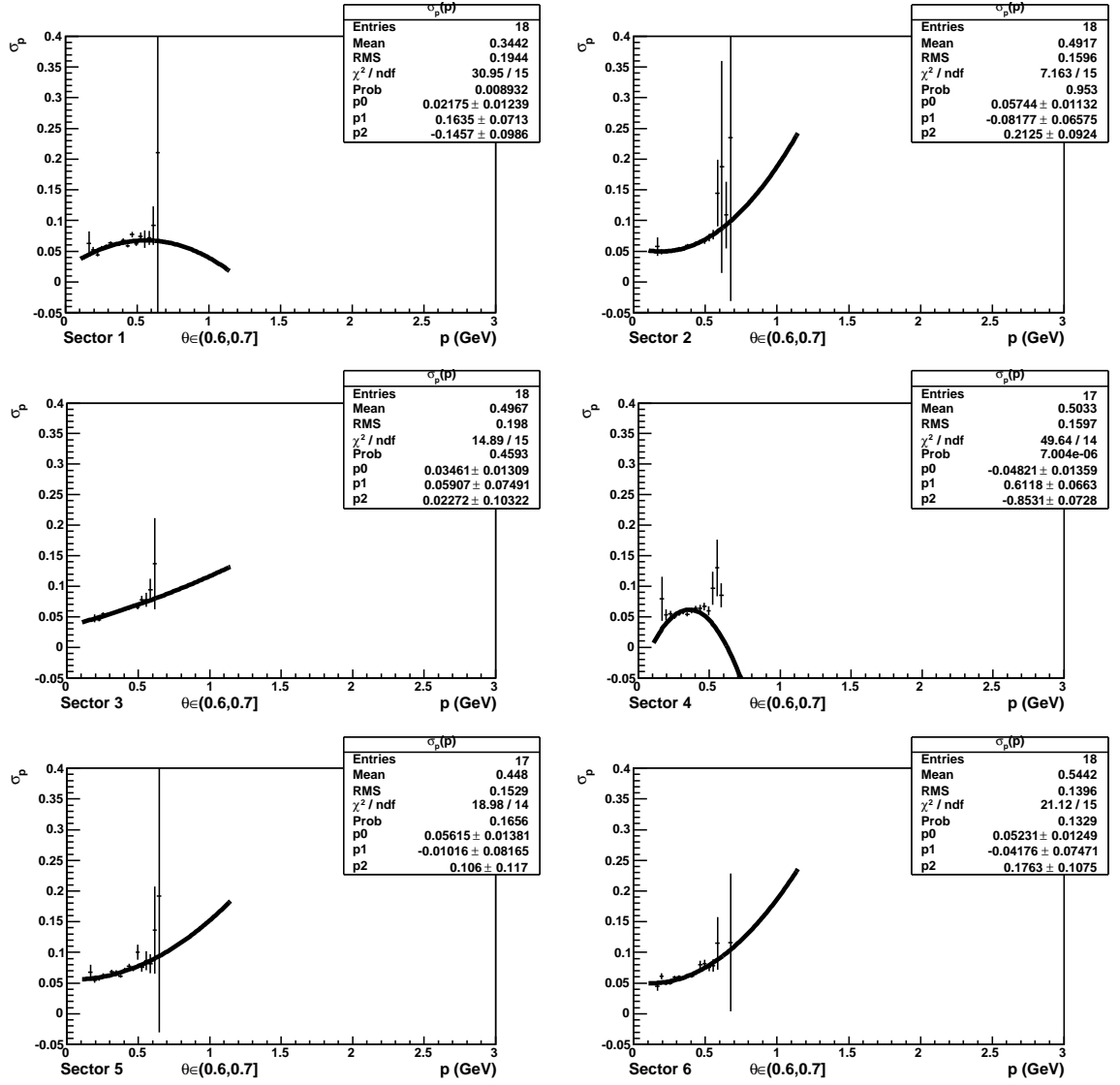
Figure 42: The Monte Carlo momentum resolution σ_p for each CLAS EC sector for $\theta\epsilon(0.6, 0.7]$ with a quadratic fit over the momentum range of 0.1-1.15 GeV.
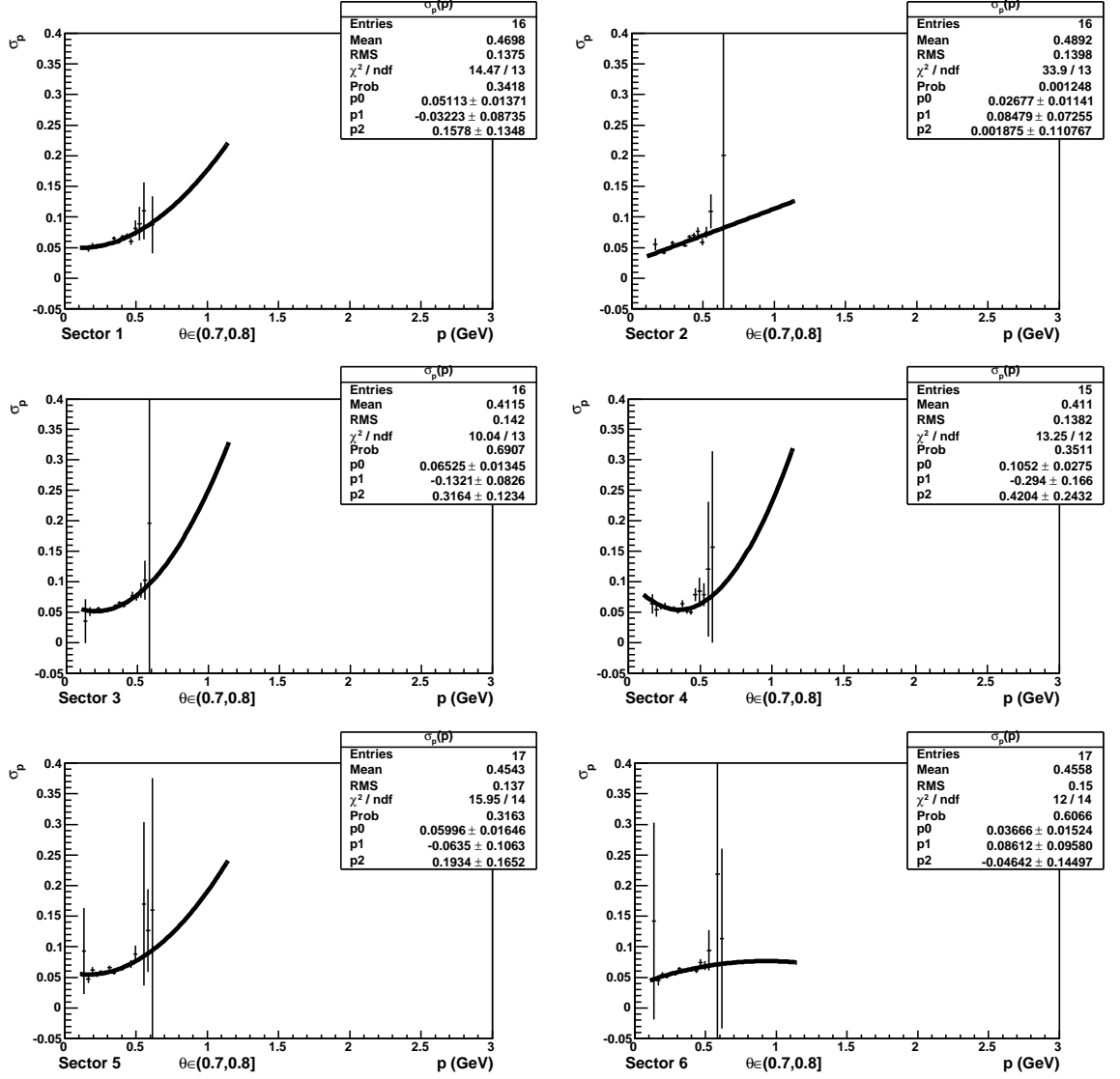
Figure 43: The Monte Carlo momentum resolution σ_p for each CLAS EC sector for $\theta \epsilon (0.7, 0.8]$ with a quadratic fit over the momentum range of 0.1-1.15 GeV.
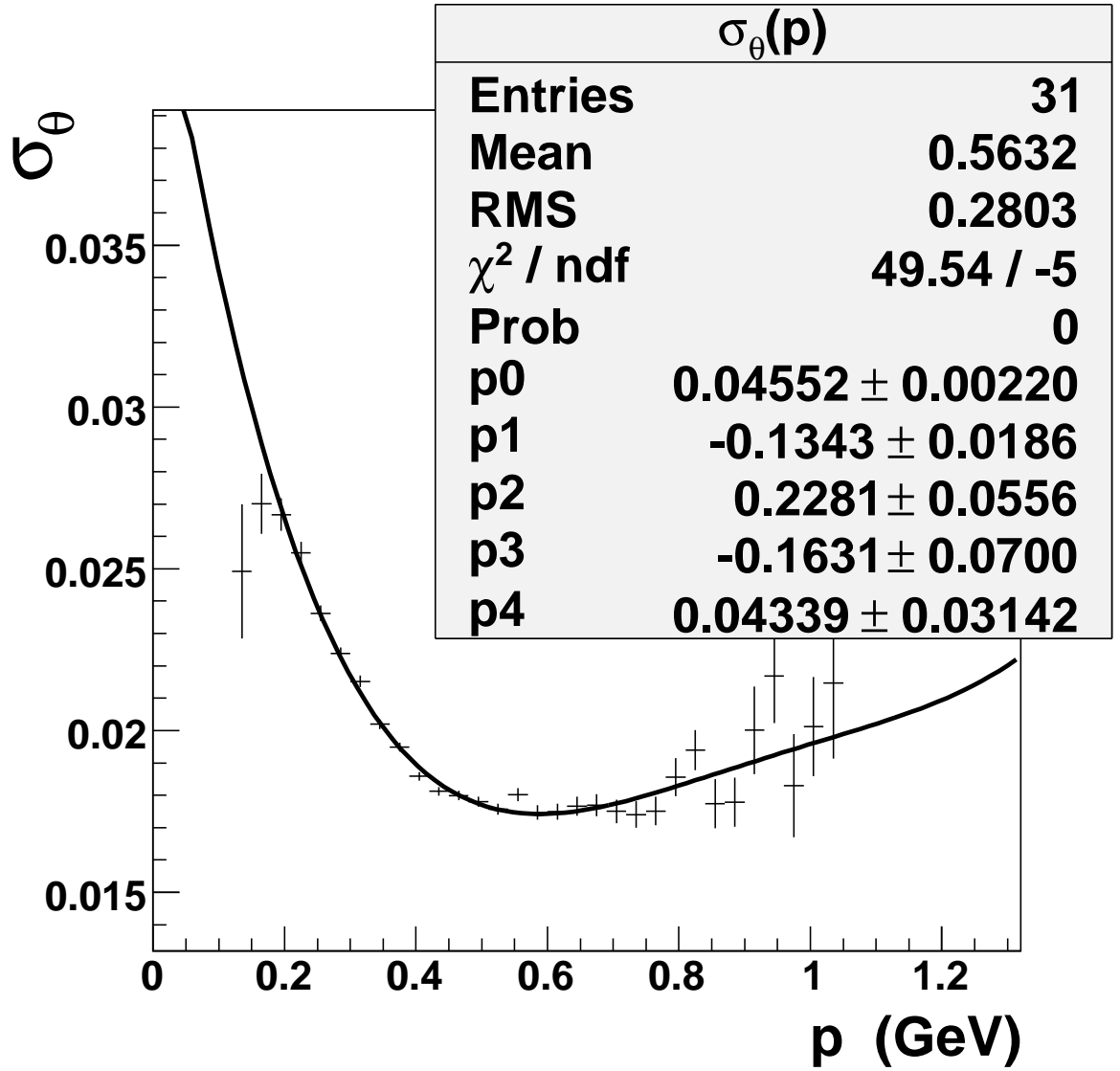
Figure 44: The $\sigma_{theta}(p)$ used to represent the variance of σ_{theta} with a four-order polynomial fit.

χ^2 / ndf	107.2 / 70
Prob	0.002808
p0	0.2464 ± 0.0071
p1	-1.238 ± 0.062
p2	2.997 ± 0.196
p3	-3.431 ± 0.263
p4	1.507 ± 0.127

χ^2 / ndf	115.9 / 69
Prob	0.0003538
p0	0.2705 ± 0.0097
p1	-1.38 ± 0.08
p2	3.355 ± 0.253
p3	-3.855 ± 0.330
p4	1.699 ± 0.157

χ^2 / ndf	73.02 / 63
Prob	0.1819
p0	0.1414 ± 0.0162
p1	-0.3961 ± 0.1562
p2	0.427 ± 0.536
p3	-0.04099 ± 0.78176
p4	-0.1203 ± 0.4101

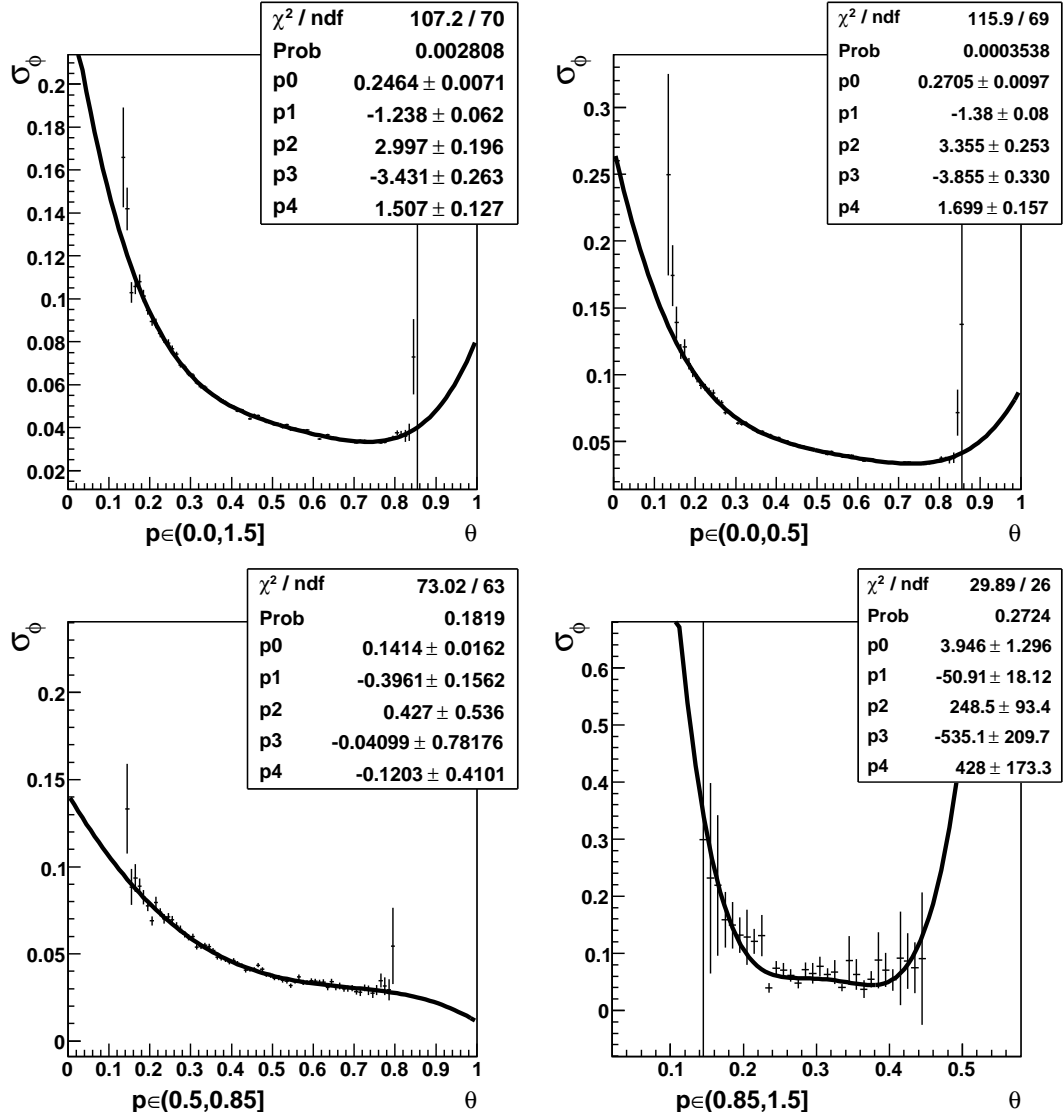| χ^2 / ndf	29.89 / 26
Prob	0.2724
p0	3.946 ± 1.296
p1	-50.91 ± 18.12
p2	248.5 ± 93.4
p3	-535.1 ± 209.7
p4	428 ± 173.3

Figure 45: The $\sigma_\phi(\theta)$ used to represent the variance in σ_ϕ for various momentum ranged. The upper left plot shows the values of σ from the Gaussian fits over the full momentum range while the upper right shows the same for momentum from 0-0.5. The bottom left shows the momentum range 0.5-0.85, and the bottom right shows from 0.85 and up (angular units in radians).
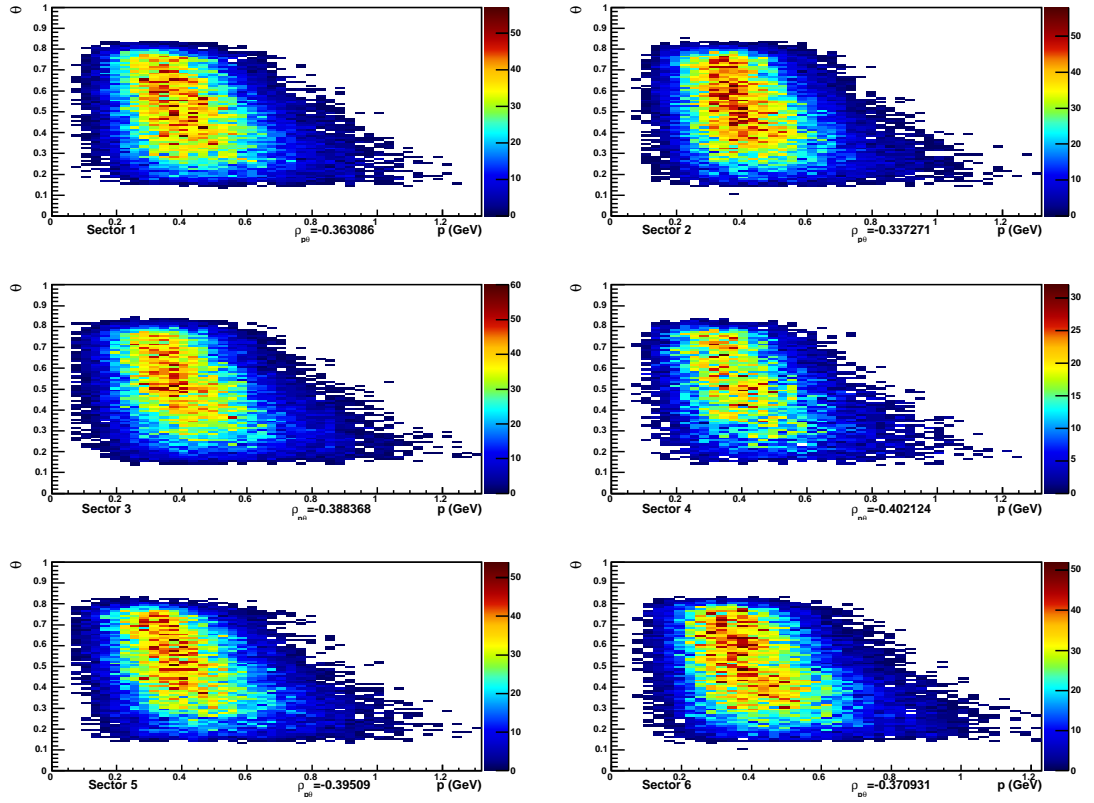
Figure 46: The measured variables p and θ are used to find the correlation ($\rho_{p\theta}$) in each CLAS sector (angular units in radians).
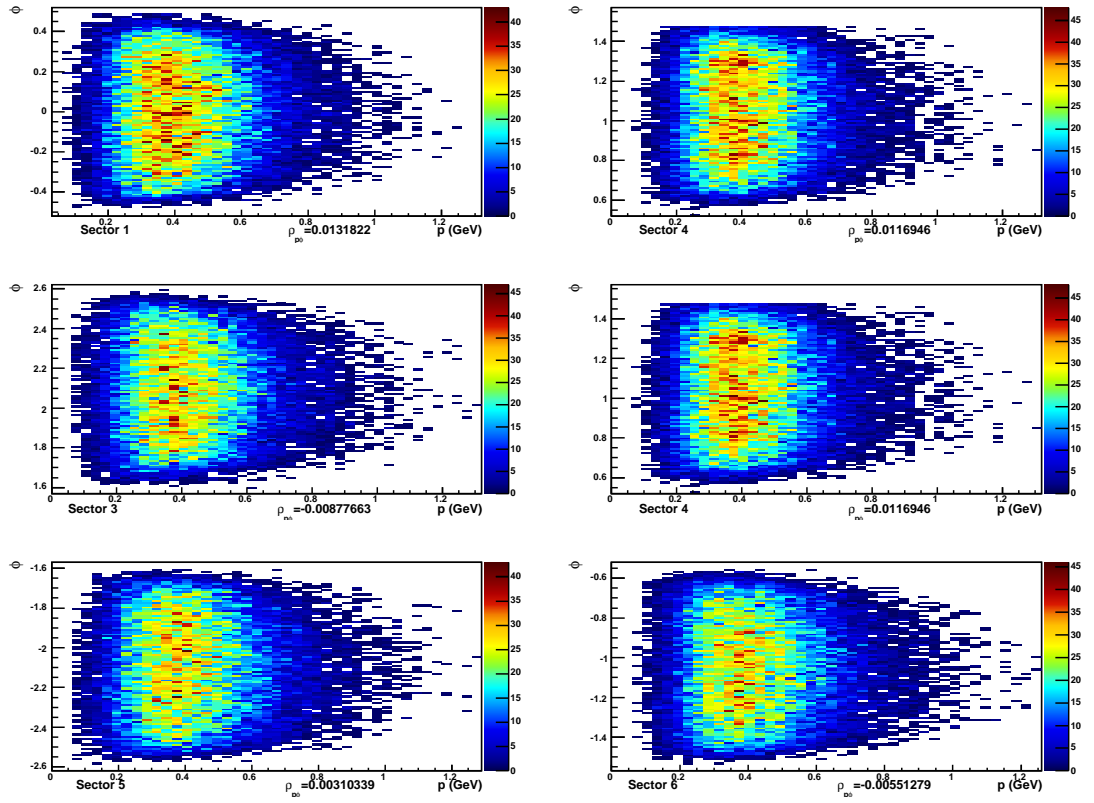
Figure 47: The measured variables p and ϕ are used to find the correlation $(\rho_{p\phi})$ in each CLAS sector (angular units in radians).
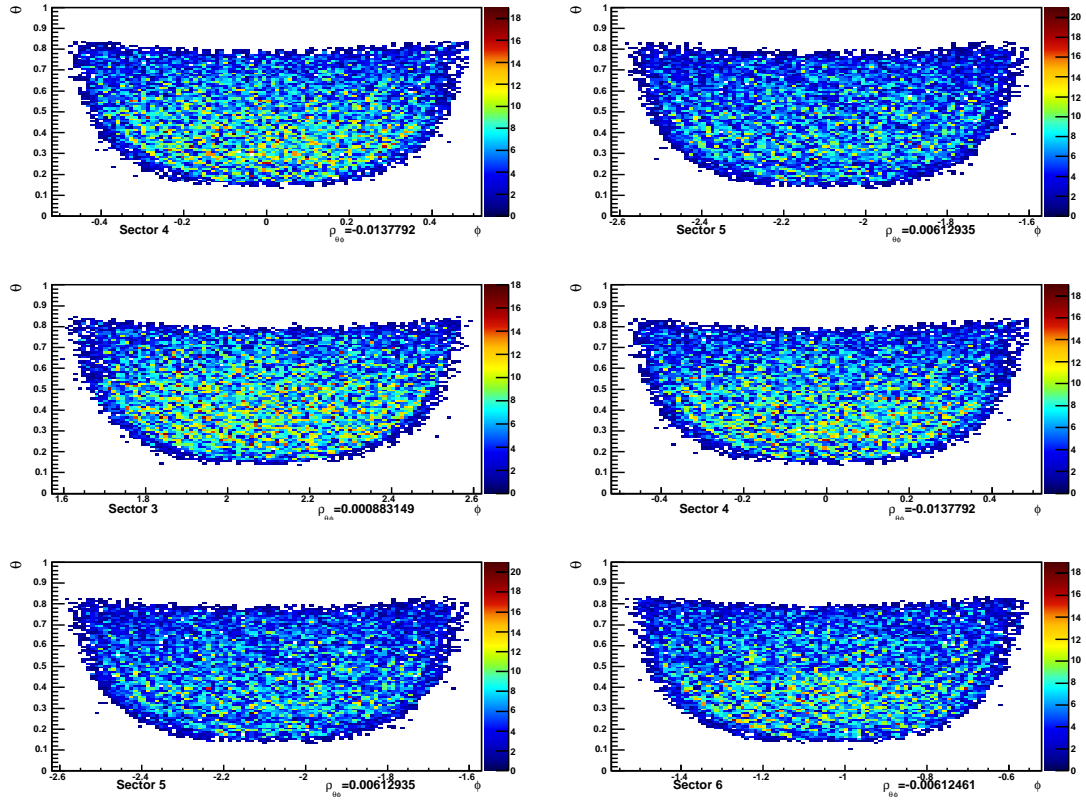
Figure 48: The measured variables ϕ and θ are used to find the correlation ($\rho_{\phi\theta}$) in each CLAS sector (angular units in radians).
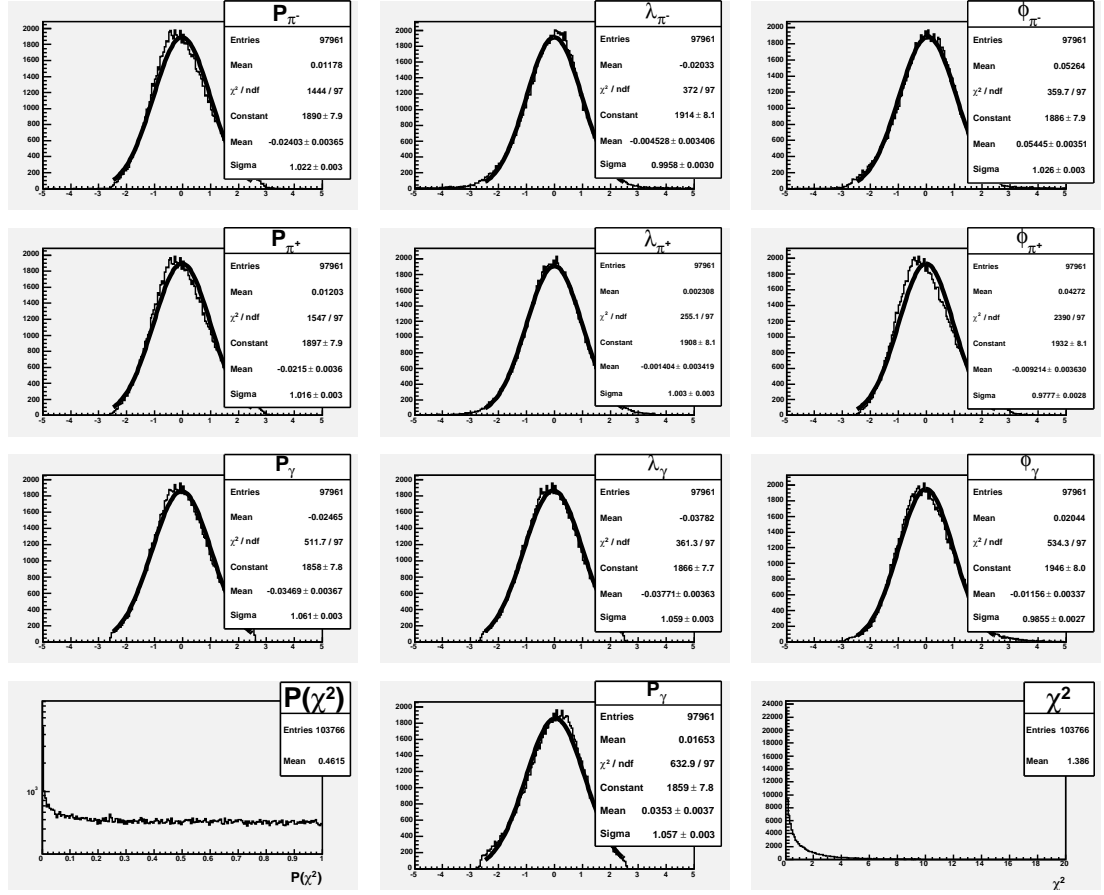
Figure 49: The Pull distribution for a kinematic fit using the photon resolutions for the channel $\gamma p \to \pi^- \pi^+ \gamma(p)$, no EC fiducial cuts were used.

References

[1] D. Keller "Techniques in Kinematic Fitting", CLAS-NOTE, Jefferson Lab, 2010-015.

[2] D. Keller "EC neutron Covariance", CLAS-NOTE, Jefferson Lab, 2011-001.

[3] Rene Brun and Fons Rademakers, ROOT - An Object Oriented Data Analysis Framework, Proceedings AIHENP'96 Workshop, Lausanne, Sep. 1996, Nucl. Inst. & Meth. in Phys. Res. A 389 (1997) 81-86. See also http://root.cern.ch/.